Hydrothermal sediments record changes in deep water oxygen content in the SE Pacific

Rachel A. Mills, Sarah L. Taylor, Heiko Pälike and John Thomson

National Oceanography Centre, University of Southampton, European Way, Southampton, SO14 3ZH, UK

Abstract

The distribution of redox-sensitive metals in sediments is potentially a proxy for past ocean ventilation and productivity, but deconvolving these two major controls has proved difficult to date. Here we present a 740 kyr long record of trace element concentrations from an archived sediment core collected at ~15^{o}S on the western flank of the East Pacific Rise on 1.1 Ma old crust, and underlying the largest known hydrothermal plume in the world ocean. The downcore trace element distribution is controlled by a variable diagenetic overprint on the inferred primary hydrothermal plume input. Two main diagenetic processses are operating at this site: redox cycling of transition metals and ferrihydrite to goethite transition during aging. The depth of oxidation in these sediments is controlled by fluctuations in the relative balance of bottom water oxygen and electron donor input (organic matter and hydrothermal sulfides). These fluctuations induce apparent variations in the accumulation of redox-sensitive species with time. Sub-surface U and P peaks in glacial age sediments, in this and other published data sets along the Southern EPR, indicate that basin-wide changes in deep ocean ventilation, in particular at

glacial-interglacial terminations II, III, IV and V, alter the depth of the oxidation front in the sediments. These basin-wide changes in the deep Pacific have significant implications for carbon partitioning in the ocean-atmosphere system and the distribution of redox-sensitive metals in ridge crest sediment can be used to reconstruct past ocean conditions at abyssal depths in the absence of alternative proxy records.

Index terms: Paleoceanography (0473, 3344), geochemical tracers (4924), glacial (4926), interglacial (4936)

1. Introduction

Hydrothermal sediments derived from plume dispersion of vent derived particles accumulate around tectonically-active margins such as mid-ocean ridges [*Mills and Elderfield*, 1995], but are rarely exploited for paleoceanographic reconstruction of past ocean conditions because of the complexity of inputs and post-depositional changes in these sediments. Iron-oxide hydrothermal particles co-precipitate certain trace elements (e.g. U, Mo, As, P, V) from seawater [*Edmonds and German*, 2004; *Feely et al.*, 1996] and many trace metals (e.g. Fe, Cu, Zn, U, Mo, Cd, Pb) are enriched in sulfide particles which are transported along with the Fe oxides [*Trocine and Trefry*, 1988]. The sedimentary record of these elements depends on the nature and extent of post-depositional reactions at the seafloor [*Poulton and Canfield*, 2006]. The trace element record in metalliferous sediments can potentially reveal past changes in ocean chemistry if the seawater record is preserved [*Edmonds and German*, 2004; *Feely et al.*, 1996], but problems in interpretation arise because the record can be perturbed during suboxic

diagenesis [*Schaller et al.*, 2000] and low-temperature fluid flow [*Mills and Dunk*, 2010]. Furthermore, in sediments with low accumulation rates, bioturbation and sediment redistribution smooth the record of past changes.

In the abyssal South Pacific the sediment records are significantly impacted by hydrothermal inputs, and generating a record of past change in this setting has remained a challenge. The Southern East Pacific Rise (SEPR) between 13 and 18^{o}S is a site of intense hydrothermal activity [*Lupton and Craig*, 1981], and particle-rich plumes are present along more than half of the ridge axis in this region [*Feely et al.*, 1996]. The metalliferous sediment distribution in this region of the SE Pacific is controlled by westward flow at ~2500 m depth [*Reid*, 1982] which transports the hydrothermal plume over hundreds of km [*Dymond*, 1981]. Systematic downcore variation in oxyanion [*Poulton and Canfield*, 2006] and trace metal [*Schaller et al.*, 2000] content has been observed in young crustal and ridge flank sediments from this sector. In particular, subsurface uranium concentration peaks are common along the EPR from 10^{o}S [*Schaller et al.*, 2000] to 20^{o}S [*Shimmield and Price*, 1988] (Fig. 1). The origin and implications of these subsurface uranium enrichments in EPR sediments have been debated over several decades but not satisfactorily explained. Subsurface enrichments have previously been attributed to diffusive uranium uptake from seawater and fixation in suboxic sediments under higher productivity glacial conditions [*Yang et al.*, 1995], scavenging of seawater uranium by variable inputs of reactive hydrothermal plume particles [*Shimmield and Price*, 1988] and within-sediment transport [*Mills and Dunk*, 2010] and precipitation from uranium-rich fluids [*Rydell et al.*, 1974; *Schaller et al.*, 2000]. Deciphering the

origin of these uranium peaks would provide new information for an ocean region with sparse Pleistocene proxy records.

Volumetrically the deep Pacific Ocean makes up a significant proportion of the global ocean and thus changes in Pacific circulation, ventilation and deep water nutrient, and carbon content can have a major impact on biogeochemical cycles. Most late Pleistocene reconstructions of the Pacific have focussed on productivity variations [e.g. *Martinez and Robinson,* 2009] and changes to ventilation of the upper water column [e.g. *Stott et al.,* 2009]. Recent combined proxy and modelling approaches suggest reorganisation of the North Pacific deep water ventilation during the last glacial termination may have had a significant impact on global heat transfer [*Okazaki et al.,* 2010] but there are limited proxy records to test this hypothesis, particularly in the south Pacific.

Paleoceanographic records from the SE Pacific are sparse because carbonate sedimentation is restricted to the hydrothermally-dominated ridge region. The published sedimentary records along the EPR lack age models and often the depth sampling resolution is inadequate. Our knowledge and understanding of past change would be significantly enhanced if the hydrothermal plume input and post-depositional changes within the sediment record could be deciphered and interpreted to reconstruct paleoceanographic and paleoclimatic conditions for this ocean.

Here we present new age controlled data for an archived sediment core originally studied by *Rydell et al.* [1974] that demonstrates that diagenetic overprinting of hydrothermal inputs from the SEPR records significant glacial-interglacial changes in ventilation of the deep ocean moderated by intense redox cycling at glacial terminations II, III, IV and V

during the Pleistocene. Comparison with published records along the SEPR suggests that these changes were basin wide and may thus significantly impact the storage of respired carbon in the deep ocean and poleward oceanic heat transport.

1.2 Paleoceanographic Setting

The EPR ridge-crest from 10 to 20°S underlies low-productivity oligotrophic subtropical waters and is bathed by North Pacific Deep Water (NPDW: T <2°C, O_2 <150 μM [*Fiedler and Talley*, 2006]) which recirculates southwards from the North Pacific as the major return flow of the overturning circulation in this basin. This water mass underlies the well-ventilated intermediate modal waters sourced from the Southern Ocean [*Fiedler and Talley*, 2006]. The nutrient maximum and oxygen minimum associated with the modern NPDW outflow is centred at ~2000 m depth in the modern ocean. This return flow is hypothesized to have deepened to 2500-3000 m depth during the Last Glacial Maximum [*Sigman and Boyle*, 2000; *Matsumoto et al.*, 2002] sequestering nutrients and respired carbon to the abyss and thus lowering atmospheric pCO_2 [*Boyle*, 1988]. This hypothesis has been tested extensively by attempts to reconstruct glacial Pacific nutrient distributions but has been hampered by apparently contradictory proxy records (e.g., $\delta^{13}C$ [*Matsumoto et al.*, 2002] and Cd/Ca [*Boyle,* 1992]). Redox-sensitive metal records have been used in various ocean basins to identify glacial decrease in abyssal water oxygen content [e.g., *Galbraith*, 2007]. These different proxy records have recently been reconciled by the identification of an enhanced glacial respired carbon pool in the deep NW Pacific with lower oxygen levels but unchanged phosphate content arising from shifts in preformed nutrient supply [*Jaccard et al.*, 2009].

Glacial terminations are the times when the strongest changes in deep water ventilation and thereby oxygen levels, sedimentation rates, and input of electron donors occurs [*Broecker and Denton*, 1989]. Glacial terminations with global evidence for reconfiguration of ocean circulation occur at the ends of Marine Isotope Stage (MIS) 12 (V), 10 (IV), 8 (III), 6 (II) and 2 (I). There is evidence from the Pacific for basin-wide maxima in export production during early deglaciation which in turn impacts on bottom water oxygen content [*Martinez and Robinson*, 2010]. The inferred deglacial shifts in deep Pacific ventilation will also have significant controls on abyssal water oxygen levels *[Okazaki et al., 2010]*.

At glacial terminations where benthic redox processes are perturbed, nonsteady-state diagenetic processes are initiated which lead to post-depositional diagenetic overprint within these sediment intervals [*Thomson et al.*, 1996]. Sedimentary redox driven diagenesis occurs throughout the redox gradient surrounding the oxidation front [*Thomson et al.*, 1996]. Here we use the term oxidation front in a general way to describe the region just above and just below the limit of oxygen penetration, where a range of elements undergo redox cycling at different levels within the sediment in response to rapidly changing redox conditions. Solid phase Mn(IV) accumulates above the oxidation front in oxic conditions, supplied by reduced Mn(II)(aq) from below. Conversely solid phase, authigenic U(IV) accumulates under post-oxic conditions within the oxidation front, supplied by dissolved U(VI) from above. Several other redox-sensitive elements are mobile and reactive within the oxidation front and can form local enrichment peaks between those of Mn and U [*Thomson et al*., 1996].

2. Sampling and methods

The core GS7202-35 was recovered from 82 km west of the EPR ridge axis at 14°47.9'S, 113°30.1'W from a water depth of 3044 m and comprised trigger and piston cores 1.7 m and 8.47 m in length, respectively [*Rydell et al.*, 1974]. The cores are archived in the Miami Core Repository at 4°C and were resampled in contiguous 5 cm strips (~4 kyr increments) which were dried, ground and homogenised prior to geochemical analysis. Bulk carbonate $\delta^{18}O$ and $\delta^{13}C$ were measured on a Europa Scientific GEO 20-20 mass spectrometer and all data are expressed relative to the VPDP standard. Carbonate and organic carbon content were determined by difference using coulometry and by Carlo Erba CHN analysis. Major (Fe, Mn, Ca, Al, Si, Ti, P, K, Na) and trace element analyses (U, Mo, Cd, V, Cu, Ba, Br, I, S, Cl) were carried out using a Philips PW1400 fully automatic wavelength dispersive XRF. A subset of 25 samples was subjected to a total digestion procedure (*Dunk and Mills*, 2006) for analysis by Inductively Coupled Plasma-Atomic Emission Spectrometry. Analysis was carried out on a Perkin Elmer Optima 4300DV Precision ICPAES. Accuracy of these ICPAES analyses was assessed by comparison with USGS standard MAG-1 and was better than 1%. XRF pellets were calibrated using matrix-matched standards comprising mixtures of USGS standards MAG-1, JLs-1, GXR-1, NIM-L, BE-N, SDo1, NOD-P-1 and NOD-A-1. Accuracy of the XRF analysis was also assessed by comparison with the ICPAES data and for all elements presented (Table 1) is better than 3% of the certified value.

We avoid issues relating to variable carbonate dilution downcore by reporting elemental ratios; all ratios are expressed in mass units (g/g). A comparison of the bulk sedimentary trace element/Fe ratios with the SEPR plume [*Feely et al.*, 1996] and oxic metalliferous sediments from east of the ridge axis at the same latitude [*Dunk and Mills*, 2006] (Figs.

4d; 7a-d) allows assessment of the inputs and post-depositional changes occurring with time. All data are for bulk sediment analysis including dried pore water salt.

3. Results and Discussion

3.1 Age model and sediment accumulation

The trigger and piston cores were combined into one continuous record using a combination of the downcore bulk $\delta^{18}O$ and trace element profiles. The best Pearson correlation for all records was achieved when the piston and trigger core were overlapped by 27.5-32.5cm; all piston core depths have therefore been adjusted by +135.25 cm relative to the published stratigraphy which assumed erroneously that the piston core sampled the sediment water interface [*Rydell et al.*, 1974]. An age model for the sediment accumulation was constructed by correlation of the bulk sediment $\delta^{18}O$ record with the astronomically-tuned composite time series obtained from cores V19-30, ODP 677 and ODP840 [*Shackleton et al.*, 1990] using the Analyseries software [*Paillard et al.*, 1996]. We estimate the uncertainty of the correlation to be <10 kyr, with a clear identification of all glacial and interglacial periods in the records (Fig. 2a).

The 9.8 m combined core contains a 740 kyr record which spans Marine Isotope Stages (MIS) 1 to 20 [*Shackleton et al.*, 1990] with linear sedimentation rates (LSR) of 0.95-1.64 cm ky^{-1} (Fig. 2c). There is no systematic glacial-interglacial change in inferred LSR but there is a notable decrease in LSR at the end of MIS 7, when the core location was ~68 km from the ridge axis. The lower sedimentation rate in the upper core (~1 cm kyr^{-1}) means that glacial-interglacial differences are not as clearly resolved as those deeper in the core. The observed sedimentation rates are consistent with estimates from $^{230}Th_{xs}$

decay in the upper 3 mbsf [*Rydell et al.*, 1974] and estimated mean accumulation from seismic profiling [*Hauschild et al.*, 2003]. At 15^{o}S the sediment appears to drape the seafloor uniformly with little indication of lateral sediment transport [*Hauschild et al.*, 2003]. There is little basement topographic variation and therefore minimal basal fluid advection through the sediment on this ridge flank compared with the eastern flank at this latitude [*Mills and Dunk*, 2010]. Based on estimated spreading rates [*Grevemeyer et al.*, 2002], core GS7202-35 was located ~25 km west of the EPR axis at 740 ka and has moved a further 57 km off axis since that time.

Pleistocene sedimentary records are characterised by the mid-Pleistocene transition (MPT) which is manifest in the Pacific by significant changes in the bulk carbon isotope composition (Fig. 2b; [*Shackleton and Hall*, 1995]) and marked shifts in the inferred deep water ventilation by the South Pacific upper circumpolar deep water (UCDW) at 870ka and 450ka [*Venuti et al.*, 2007]. The early deposition at site GS7202-35 (740-400 kyr) occurred during the MPT. The major shift in bulk carbon isotope composition recorded in Equatorial Pacific sediment has been interpreted as evolutionary succession in the nanofossil assemblage [*Shackleton and Hall*, 1995]. The bulk δ^{13}C record for this core exhibits the main features seen in the Equatorial Pacific Pleistocene record, providing additional stratigraphic constraints for the proposed age model (Fig. 2b). There is evidence for a number of shorter-lived shifts in carbon isotope partitioning at this site at the ends of MIS 12, 10 and 8 (Teminations V, IV and III; Fig. 2b).

3.2 Sediment composition

The sediment of core GS7202-35 comprises a mixture of hydrothermal material derived from plume fallout (Fe sulfides and Fe and Mn oxyhydroxides) and biogenic carbonate ($CaCO_3$) with minor biogenic silica and aluminosilicates (Table 1; Fig. 3). The maximum lithogenic (basaltic) input at this site estimated from the bulk sediment Al content and the Al content of basalt at this latitude (Al = 8.88% [*Schramm et al.*, 2005]) is small (0.52-1.57% of bulk sediment) and this component can be ignored in our discussion. Note that the highest basaltic inputs are observed towards the base of the core when the site was closer to the ridge axis. The biogenic carbonate content varies from 58-72% (Fig. 4a) with lower values in the deeper parts of the core that are diluted by the more intensive hydrothermal input (up to 40%) when the core location was closer to the ridge axis. The main control on $CaCO_3$ burial away from the equatorial productivity maximum is inferred to be carbonate preservation rather than changes in productivity [*Murray et al.*, 2000; *Anderson et al.*, 2008]. The characteristic changes in $CaCO_3$ preservation are damped at the shallow ridge-crest and the dramatic glacial-interglacial fluctuations seen elsewhere in $CaCO_3$ records in Pacific cores retrieved from greater water depths (>4200 m, [*Murray et al.*, 2000]) are not observed in this shallower ridge flank 15^{o}S record. However, the significant dissolution event associated with MIS 11 [*Murray et al.*, 2000] is associated with a minima in $CaCO_3$ content in this record (Fig 4a). The hydrothermal material preserved in the sediment largely consists of X-ray amorphous Fe and Mn oxides with a minor clay component (<1%). Consideration of the sea salt elements S, Na, Cl, Br indicate the presence of 100-2500 ppm excess S content relative to Cl throughout the core, and Fe sulfides have been observed by scanning electron microscopy of impregnated sections of sediment from the ridge crest at this

latitude [*Dunk and Mills*, 2006]. So whilst sulfide oxidation will have occurred during 25 years of core storage, the presence of primary sulfides at this site is inferred from the excess S measured by XRF. The organic carbon content of the sediment is low throughout (<0.2%) with no measurable variation with depth; these low values are consistent with published data from this oligotrophic region [*Schaller et al.*, 2002].

Plume particles collected from the neutrally-buoyant plume overlying the super-fast spreading EPR consist of a mixture of Fe and Mn oxides and sulfide/elemental sulfur phases [*Feely et al.*, 1996]. Plume particles collected from the neutrally-buoyant plume ~25km west of the ridge axis at 15^{o}S contain significant particulate sulfur (~30 nmol/L; particulate molar S/Fe ~ 0.04) and particulate Mn (1-2 nmol/L; particulate molar Mn/Fe up to 0.1 [*Feely et al.*, 1996]). Plume particles collected from further south on the EPR contain a particulate component characterised by high levels of reduced S, particulate Mn and methane [*Feely et al*., 1996]. Plume transported hydrothermal sulfides are inferred to contribute significant transition metals to sediments from 10^{o}S and elsewhere on the EPR [*Schaller et al.*, 2000; *Poulton and Canfield*, 2006]. Thus the two sources of electron donor to the sediment at this site are organic carbon export from overlying oligotrophic waters and hydrothermally-derived reduced sulfur species. The electron donor input to the sediment is inferred to be cyclical, either through glacial-interglacial variation in overlying productivity and carbon export or by variations in hydrothermal inputs from the EPR which in turn are moderated by bottom water oxygenation which is determined by abyssal ventilation rates.

3.3 Fe and Mn diagenesis

The core is highly enriched in Fe (4.2-12%) and Mn (1.4-6.9%) throughout (Table 1; Figs. 3 and 4b, c). The Fe content co-varies inversely with the $CaCO_3$ content (Fig. 3) so that the dominant control on Fe content is the variable dilution with $CaCO_3$ downcore. Mn/Fe ratios are variable and high (0.24–0.47; Fig. 4d). These values are higher than oxic sediments east of the axis at this latitude (EXCO: Mn/Fe = 0.21–0.33 [*Dunk and Mills*, 2006]) and elsewhere on the EPR (10^oS: 0.17-0.33 [*Schaller et al.*, 2000], 20^oS: 0.29-0.35 [*Shimmield and Price*, 1988]). These Mn/Fe ratios are also higher than the inferred hydrothermal sediment endmember calculated for Nazca Plate metalliferous ridge-crest and flank sediments (Mn/Fe = 0.323; [*Dymond*, 1981]) throughout the core below 25 cmbsf, although Mn/Fe values approach this modern sedimentary endmember value at glacial terminations V, IV, III and II (Fig. 4d). The source of additional Mn is inferred to be the hydrothermal plume inputs associated with super-fast spreading hydrothermalism as characterised by Mn- and S-rich particles collected on the SEPR [*Feely et al*., 1996].

Dissolved Mn(II) is the product of dissimilatory Mn reduction during early diagenesis and Mn(II) can also be derived from *in situ* reaction of Mn oxides with plume-derived sulfides [*Aller and Rude*, 1988; *Schippers and Jørgensen*, 2001]. The resultant Mn(II) is retained within the sediment both by sorption on carbonate surfaces and reprecipitation as diagenetic Mn(IV) phases in the oxic surface layer [*Shimmield and Price*, 1986; *Thomson et al.*, 1986; *Yang et al.*, 1995]. The relatively high Mn/Fe ratios compared with ridge-crest and flank sediments from 10^oS [*Heath and Dymond*, 1981; *Schaller et al.*, 2000] indicate that the oxic surface layer at this site must always have been thick enough to trap a significant proportion of the upwardly diffusing Mn within the sediment for most of the

last 740 ka. This is in contrast to sediment records from 10°S, 34km from the ridge axis, where significant Mn loss is observed below 4 cmbsf (Mn/Fe = 0.17-0.33; [*Schaller et al.*, 2000]). There is no Mn redox cycling apparent in oxic sediments from the same latitude east of the ridge axis; sedimentary Mn/Fe ratios are relatively constant and no measurable Mn^{2+} is observed in pore waters [*Dunk and Mills*, 2006] although inferred carbon export and bottom water oxygen [*Fiedler and Talley*, 2006] is similar east and west of the ridge axis at 15°S. Thus the main control on redox status at the EPR sites is inferred to be the enhanced hydrothermal supply of reduced sulfide species on axis and the western flank that are subsequently oxidised *in situ* during early diagenesis.

Hydrothermally-derived Mo is associated with hydrothermal sulfides which are transported to the ridge-crest and flank sediments. *In situ* oxidation of sulfides releases Mo to pore waters and the Mo content of post-oxic sediments is subsequently controlled by the redox cycling of Mn within the oxidation front [*Schaller et al.*, 2000]. The molybdate oxyanion (MoO_4^{2-}) has a high affinity for MnO_2 and Mo is remobilised when the MnO_2 substrate is reduced during early diagenesis [*Shimmield and Price*, 1986]. The Mo/Mn ratio of oxic deep sea sediments and ferromanganese deposits is relatively constant (0.002; [*Shimmield and Price*, 1986]) and the average ratio for oxic sediments (with lower hydrothermal Mn content) from the eastern EPR flank at 15°S is 0.0016 [*Dunk and Mills*, 2006]. The Mo/Mn ratio at 15°S does not reach oxic values at any depth within the core (Fig. 4e). The hydrothermal supply of particulate Mn at this site [*Feely et al.*, 1996] vastly exceeds the inferred Mo supply which is not adequate to achieve normal pelagic oxic Mo/Mn ratios even within the upper oxic layers: Mn is significantly enriched throughout the core. The low downcore Mo/Mn ratio indicates that

significant Mn cycling (and preferential Mo loss) occurred while the core was relatively close to the ridge axis under post-oxic conditions and Mo remobilisation and accumulation in the upper core is apparent (Fig. 4e). The elevated Mo/Mn ratios in the upper core are consistent with a shift to more oxic sedimentary conditions with time which is inferred to relate to the distal accumulation of more oxidised hydrothermal material and an overall increase in Pacific ventilation and/or decrease in carbon export since the mid-Pleistocene transition [*Venuti et al.*, 2007].

The active oxidation front in this core is inferred to be at ~140 cmbsf (120 kyr; Fig. 4e) based on the Mo distribution and the maximum inflection in the Mo/Mn profile. The shape of the Mo/Mn profile is consistent with progressive deepening of the oxidation front to 140 cmbsf and Mo preferentially accumulates above oxidation front over time as continued Mo and Mn cycling occurs. Metastable remnants of relict Mo/Mn peaks are observed in MIS 7 and 9 (Fig 4e). Deep (>1 m) oxidation fronts have previously been identified in Atlantic cores where non-steady state diagenesis is controlled by turbidite emplacement with additional organic carbon supply to the seafloor [*Colley and Thomson*, 1985] and deep oxygen penetration (several metres) is observed in hydrothermal sediments collected from the same latitude on the eastern flank of the EPR [*Dunk and Mills*, 2006]. Cores underlying the oligotrophic South Pacific gyre show oxygen penetration to basement (~8m depth; [*Fischer et al.*, 2009]). The slow sediment accumulation in the upper core and the inferred low electron donor input relative to deeper in the core mean that while similar processes may well occur transiently at the end of MIS 2 (termination I), evidence for non-steady state redox cycling is not preserved in

the upper sediment record and the active oxidation front has now penetrated to termination II (140 cmbsf).

Plume-derived hydrous Fe oxides which include ferrihydrite phases will undergo transformation during oxic and suboxic diagenesis to a range of more crystalline Fe rich phases [*Dunk and Mills*, 2006]. Phase transformation reactions exclude large cations and oxyanions from the more crystalline Fe oxide structures and diffusive transport and reaction of these elements can overprint the primary sedimentary record. The *in situ* oxidation of Fe sulfides by a range of electron donors including O_2, NO_3^- and MnO_2 [*Aller and Rude*, 1988] leads to ferrihydrite formation during early diagenesis and this ferrihydrite transforms to crystalline phases over time, further complicating the diagenetic history of this core.

3.4 Trace metal diagenesis

The U content in core GS7202-35 is extremely high compared with normal hydrothermal sediments (Fig. 5a) with maximum values found consistently in sediments laid down during glacial periods, and a peak of 30 ppm at 6.33 mbsf (443 kyr, MIS 12). Previously published $^{234}U/^{238}U$ ratios [*Rydell et al.*, 1974] are within error of the age corrected seawater activity ratio (1.14 [*Chen et al.*, 1986]) in the upper 4.5 m of the core, indicating a seawater origin for the sedimentary U. Uranium has been shown to be elevated on hydrothermal sulfide surfaces [*Mills et al.*, 1994] and in sulfidic plume particles on the northern EPR [*German et al.*, 2002]. Thus fine-grained plume-derived sulfides are a major source of U input to metalliferous sediments.

The Cd content is also significantly elevated throughout the core (10-40 ppm; Fig. 5b), reflecting the plume sulfide input at this site. Trans-Atlantic Geotraverse (TAG) plume sulfides have Cd contents of 10-500 ppm [*Metz and Trefry*, 1993] and *in situ* oxidation of sulfides will lead to Cd association with oxyhydroxide phases and retention in the sediment. Comparison with ridge-crest cores at 10°S [*Schaller et al.*, 2000] implies that the Mo, U and Cd are all primarily sourced from sulfidic plume input and are variably mobile during suboxic diagenesis.

The U/Fe ratio for oxic ridge flank metalliferous sediments is relatively constant and low ($U/Fe = 0.3 \times 10^{-4}$; [*Mills et al.*, 1994]) and the U/Fe ratio is enhanced relative to this value throughout most of this core (Fig. 6a). At the active oxidation front (120 kyr), U is inferred to have been relocated into the underlying glacial section by oxidation [*Colley and Thomson*, 1985]. Oxygen penetration and oxidation remobilises a fraction of plume-derived U that is reprecipitated as U(IV) below the oxidation front in MIS 6 (Fig. 6a). The U/Fe peaks in the upper oxic core are inferred to be non-steady state, metastable features that result from more recent hydrothermal sedimentation during MIS1-5. The decreased plume-derived electron donor supply as the core moves off axis and the slower sediment accumulation rate (Fig. 2c) allow oxygen burn down to MIS 6. The U/Fe ratio approaches the low oxic sedimentary value towards the end of MIS 6, 8, 10 and 12 (Fig. 6a) indicating that oxic burndown and redistribution of U occurred after glacial terminations V, IV, III and II as the electron donor supply to the seafloor waned and/or the bottom water oxygen content increased during the following interglacial. Maximum U/Fe ratios occur during glacial periods and in particular the largest peak occurs at 443 ka in MIS 12 (Fig. 6a). This largest U/Fe peak coincides with the MIS 12 ventilation

minimum in the South Pacific [*Venuti et al.*, 2007] which is followed by the long, warm MIS 11 interglacial period. These mid-Pleistocene climatic extremes lead to maximal relocation of the deposited U.

Diffusive uptake and fixation as U(IV) under suboxic conditions can conceivably lead to an influx of authigenic U in slowly accumulating sediments, but bioturbation and oxidation leads to net efflux of U from the sediments [*McManus et al.*, 2005]. Significant authigenic U accumulation by this mechanism only occurs in sediments where the redox interface is within a few cm of the surface [*Morford et al.*, 2005]. The surface oxic layer thickness at 15^{o}S is inferred to have exceeded 5 cm to retain the Mn(II) within the sediment throughout much of the last 740 kyr and significant authigenic U uptake from seawater only occurs when the oxidation front is close to the sediment surface under glacial conditions. The main source of the U enrichment at 15^{o}S is likely to be derived both from allochthonous inputs of seawater U associated with sulfidic plume particles [*German et al.*, 2002] and enhanced by authigenic U uptake during glacial periods. The subsurface U peaks record periods of non-steady state diagenesis and burn down associated with post glacial decrease in electron donor supply to the sediment which is associated with increasing bottom water oxygen content. This interpretation challenges the assertion by *Rydell et al*. [1974] and *Schaller et al.* [2002] that U enrichment along this sector of the EPR arises from subsurface fluid flow. The inferred variation in redox status and impact on the Mo/Mn and U/Fe ratios over glacial-interglacial cycles is summarised schematically in Fig. 7.

Phosphorus and K content covary downcore (Fig. 5c) and peaks occur in glacial stage sediments. Copper and V content also covary with depth and are inferred to be sourced

from seawater and hydrothermal inputs and their distribution modified during early diagenesis (Fig. 5d, e). These trace metal profiles will be discussed in turn to develop an understanding of the diagenetic overprinting on the inferred primary hydrothermal input.

Phosphate is highly mobile during early diagenesis and the signature preserved is inferred to be a combination of the primary hydrothermal input overprinted by diagenetic processes. High P/Fe ratios coincide with glacial periods and lower P/Fe with interglacials (Fig. 6b). The low sedimentary P/Fe ratio at this site and at 10^{o}N (Fig. 8) compared with SEPR plume particles (P/Fe = 0.1 [*Feely et al.*, 1996]) reflects the significant sulfidic plume input to this site of particles that have little affinity for seawater PO_4^{3-} [*Feely et al.*, 1996]. These low ratios are similar to P/Fe ratios at other sites along the SEPR (0.055: [*Marchig et al.*, 1986], 0.049: [*Schaller et al.*, 2000], 0.044: [*Poulton and Canfield*, 2006]) which have also been attributed to dilution of plume-derived material with plume sulfides and P loss during oxic diagenesis that predominates in the upper sediment during interglacial periods. The higher glacial P/Fe ratios are consistent with exposure to a nutrient-rich, oxygen-depleted water mass during these periods.

The close correlation between P and K at this site is striking and the most likely phase hosting K is hydrogenous Fe-hydroxyphosphates and minor phillipsite or other zeolite generated *in situ* during early diagenesis. However, there is no mineralogical evidence for the presence of any such crystalline phase in any abundance.

Barium in hydrothermal sediments is dominantly associated with the Fe oxyhydroxide fraction with additional contributions from carbonate bound barium and biogenic barite from the upper water column [*Dymond et al.*, 1981]. The Ba/Fe ratio of the hydrothermal

input at 14°S has been determined by sequential leach analysis of metalliferous sediments (Ba/Fe = 0.013; Dunk et al., 2006) and the Ba/Fe ratio of core GS7202-35 is consistently higher than this ratio (Fig. 6c) confirming the multiple sources of this element at this site. Low Ba/Fe ratios are associated with the minima in Mn/Fe (Fig. 4d) and regions of U relocation (Fig. 6a) which are relict oxidation fronts suggesting that Ba has been significantly redistributed during Mn and Fe recycling at this site and therefore cannot be used as a productivity proxy in this setting.

Other redox-sensitive metals such as Cu and V are dominantly controlled by the recycling of MnO_2 (Fig. 6d, e). Elevated Cu/Fe and V/Fe ratios correlate with maximum Mn/Fe ratios downcore and the relict oxidation fronts indicated by minimum Mn/Fe ratios correlate with minima in the Cu/Fe and V/Fe profiles. Redox cycling of MnO_2 releases Cu and V to pore fluids and they accumulate preferentially in the oxic interglacial regions overlying the active and relict oxidation fronts. The correspondence between low Mn/Fe and V/Fe ratios has previously been seen at 10°S where low V/Fe ratios are associated with Mn loss from the suboxic ridge crest sediments [*Schaller et al.*, 2000].

3.5 Mechanisms for changing depth of the oxidation front

There are three main controls on the depth of oxidation front: bottom water oxygen content, electron donor supply, and sedimentation rate. We have demonstrated that sediment accumulation at this site does not control the observed non-steady state diagenesis at terminations V, IV, III and II (Section 3.1; Fig. 2c). Comparison of the suboxic sediment record at 15°S with elemental ratios for fully oxic sediments collected at the same latitude east of the ridge axis [*Dunk and Mills*, 2006] demonstrate the impact

of plume-derived electron donors to the seafloor at this latitude. Hydrothermally-derived electron donors have a major impact on the redox state of sediments in this region.

Studies of productivity proxies at 5°S in the SE Pacific across glacial cycles including MIS 11 and 12 suggest no systematic change in export production through time but instead identify significant shifts in lysocline depth and carbonate preservation [*Murray et al.*, 2000; *Anderson et al.*, 2008] that are due to differences in bottom water carbonate ion activity related to ocean circulation changes at ~4200 m water depth. The ridge flank setting of the core studied here is well above the modern lysocline depth of ~3500 m and significant carbonate dissolution is unlikely. Records from the equatorial Pacific imply that pulses of enhanced export occurred during glacial terminations [*Martinez and Robinson*, 2010]. Thus the primary control on oxidation front depth on the ridge flank at 15°S is likely to be glacial-interglacial changes in bottom water ventilation and oxygen content which in turn controls the supply of hydrothermal sulfides to the sediment moderated by short term pulses in carbon export to the seafloor during glacial terminations. The low CaCO3 levels in MIS 11 sediments suggest that carbonate dissolution may also occur in the surficial sediments at this time. It is not possible to quantify this dissolution effect, but it would be expected to have an effect similar to a decrease in accumulation rate in that it would lead to an increase in the oxidation depth in the sediments enhancing the apparent U accumulation.

Lower glacial oxygen levels lead to a shoaling of the redoxcline in the sediment and increased accumulation of plume-derived sulfides and associated metals at the seafloor. Pulses of enhanced carbon export during glacial terminations lead to a shallow redoxcline. Mn cycling below the oxidation front leads to remobilisation of

oxyhydroxide bound metals (Mo, Cu, V) and reaccumulation above the oxidation front. Subsequent systematic deepening of the oxidation front occurs after glacial terminations V, IV, III and II, relocating the plume-derived U into the deeper suboxic sediment. Oxidation of the remnant plume-derived sulfides *in situ* provides a reactive ferrihydrite phase that effectively sorbs elements released during Fe oxide transformation reactions.

One test of this hypothesis is comparison with data from other EPR locations with documented subsurface U enrichments (Fig. 1). Few EPR cores have a Pleistocene age model and only two records have appropriate down-core sample resolution [*Schaller et al.*, 2000; *Shimmield and Price*, 1988]. The former includes multi-element data and a comparable sediment accumulation rate (~1.4 cm kyr^{-1}; [*Schaller et al.*, 2000]) which can be compared with our data set (Fig. 8). Downcore depth profiles of U/Fe and P/Fe for the upper ~2m provide a record back to MIS 6 where the glacial age U and P peaks can be correlated between the two sites (Fig. 8) supporting the case for a wider scale impact. The 10^{o}S core is significantly more reducing (inferred active oxidation front at ~4 cmbsf) than the 15^{o}S core because it is closer to the ridge axis (higher sulfide electron donor input) and underlies more productive waters at the periphery of the gyre. Thus the U/Fe ratios are higher (more U-rich sulfides supplied to sediment, less oxygen burn down and remobilisation of U) whereas the P/Fe ratios are similar to 15^{o}S. The upper core record at 10^{o}S is dominated by redox cycling and metal flux (Mo, Mn, V) to the overlying water column [*Schaller et al.*, 2000]. The high precision organic carbon record for the 10^{o}S site (Fig. 8) is consistent with glacial shallowing of the oxidation front and enhanced preservation of the organic carbon flux to the seafloor during these periods.

Comparisons with other cores are more problematic for the reasons stated above. For example, U peaks observed at 20°S previously attributed to enhanced hydrothermal scavenging [*Shimmield and Price*, 1988] are hypothesised to be associated with termination I deglaciation but in the absence of any Fe data and a poorly constrained age model this is impossible to test without resampling the archived cores. Comparisons with NW Pacific climate records from a similar depth (3244 m) suggest that glacial deepening of the oceanic respired carbon pool is a widespread phenomenon in the Pacific [*Jaccard et al.*, 2009].

4. Conclusions

New paleoceanographic records from the SE Pacific show that MIS 12, 10, 8 and 6 were associated with significant reduction in ocean ventilation at ridge crest depth (~3000 m), followed by a recharge of the bottom water with more oxygenated water after glacial terminations V, IV, III and II. This variation in ocean ventilation leads to changes in electron donor (hydrothermal sulfide) supply to the sediment that is moderated by enhanced carbon export during glacial terminations.

The large hydrothermal plume at 15°S on the EPR is inferred to have delivered variable and decreasing amounts of particulate sulfide to the core site as it moved off axis over the last 740 ka. The main control on sedimentary accumulation of hydrothermal sulfide particles is distance from the hydrothermal source and bottom water oxygen content which in turn also controls the depth of the transition metal oxidation fronts in the sediment and the exposure time to oxidation at the seafloor. As a result only trace sulfide is now found in the sediment, and the transitory presence of sulfides in the sediments has

been inferred from the very high contents of the chalcophile elements Cu, Cd, and U. *In situ* oxidation of sulfides and authigenic U uptake leads to further overprinting the inferred primary hydrothermal signature.

After glacial terminations V, IV, III and II the ridge-crest depth Pacific is inferred to be ventilated with higher oxygen content seawater and the active oxidation front progressively burns down during interglacial periods into the underlying glacial deposits modifying the Mn, Ba, Cu, V and U distributions. Suboxic ridge-crest metalliferous sediments thus provide a Pleistocene history of past bottom water oxygen in a region that has sparse palaeoceanographic records.

Published sedimentary records from the southern EPR from 10^{o}S through to 20^{o}S exhibit subsurface U (and in some cases documented P) peaks that are largely undated (Fig. 1). We demonstrate that these subsurface peaks may also be relicts of the basin-wide changes in glacial SE Pacific ventilation, but this hypothesis remains to be tested through determination of good sediment chronologies for each site and multi-element analysis at an appropriate spatial resolution.

5. Acknowledgements

Larry Peterson is thanked for providing access to samples and for resampling core GS7202-35. Darryl Green, Ian Croudace, Andy Milton and Mike Bolshaw are thanked for their assistance with geochemical analyses at NOCS. SLT was funded by NERC studentship NER/S/A/2003/11858. We are particularly grateful to Simon Poulton and Rachel Dunk for stimulating discussions during the development of this work and to Gerald Dickens, Jess Adkins and three anonymous reviewers for extremely constructive reviews and comments.

Figure Captions

Figure 1: Map of Southern East Pacific Rise showing coring location at 15^{o}S (GS7202-35 [*Rydell et al.*, 1974]). Ridge axis cores with subsurface U enrichments are shown (Y-71-7-53P [*Dymond*, 1981; *Schaller et al.*, 2000], RIS65 and 69 [*Veeh and Boström*, 1971], EXCO [*Dunk and Mills*, 2006], V19-54 [*Bender et al.*, 1971], 154-18 [*Shimmield and Price*, 1988] along with the coring location for DSDP Leg 92, hole 598 [*Poulton and Canfield*, 2006].

Figure 2: Plots of (a) the $\delta^{18}O$ for the benthic foraminifera composite (grey line) [*Shackleton et al.*, 1990] with the bulk $\delta^{18}O$ data for this study (black dots and solid line), (b) the bulk $\delta^{13}C$ composition for ODP leg 138 eastern equatorial Pacific (grey line) [*Shackleton and Hall*, 1995] with the bulk $\delta^{13}C$ data for this study (black dots and solid line), (c) the Linear Sedimentation Rate (LSR) inferred from the age model presented in (a). Distance from ridge axis is estimated from sediment age and spreading rates [*Grevemeyer et al.*, 2002]. Grey shading indicates glacial stages, numbers indicate marine isotope stages (MIS [*Imbrie et al.*, 1984]).

Figure 3: Plot of Fe (%), Mn (%), Si (%) and Al (%) against $CaCO_3$ content for core GS7202-35.

Figure 4: Plot of (a) $CaCO_3$, (b) Fe, (c) Mn, (d) Mn/Fe ratio and (e) Mo/Mn ratio against age. Dashed horizontal lines indicate the endmember hydrothermal Mn/Fe ratio for Nazca Plate ridge crest sediments [*Dymond*, 1981] and oxic sediment Mo/Mn ratio

[*Shimmield and Price*, 1986; *Dunk and Mills*, 2006]. Arrows indicate glacial terminations and the active and relict oxidation fronts (see text).

Figure 5: Plot of (a) U against age, (b) Cd against age, (c) P (open circles) and K (filled circles) against age, (d) Cu against age and (e) V against age. All shading as for Fig. 2.

Figure 6: Elemental ratio plots for core GS7202-35 plotted against age. (a) U/Fe ratio (g/g), (b) P/Fe ratio (g/g), (c) Ba/Fe ratio, (d) V/Fe ratio (g/g), and (e) Cu/Fe ratio (g/g). Arrows indicate regions of U burn down and the active and relict oxidation fronts (see text). Dashed lines indicate the U/Fe ratio for oxic metalliferous sediments [*Mills et al.*, 1994], Ba/Fe for the plume-derived component of EXCO sediments [*Dunk and Mills*, 2006], V/Fe for oxic EPR sediments [*Dunk and Mills*, 2006], Cu/Fe for the oxic SEPR endmember [*Dymond*, 1981] and oxic EPR sediments [*Dunk and Mills*, 2006]. Shaded area in (b) indicates the range in observed P/Fe for SEPR sediments (see text). All other shading as for Fig. 2.

Figure 7: Schematic representation of pore water and solid phase response to an interglacial-glacial-interglacial transition through time from left to right. Interglacial oxygen penetration is relatively deep and Mn^{2+}, and other redox-sensitive metals and those associated with Fe-Mn oxyhydroxide phases, are recycled below this depth. The glacial shift to a shallower oxidation front leads to significant Mn and Mo remobilisation from the solid phase and relocation of these elements above the new oxidation front. Differential mobility of Mn and Mo, and the significant hydrothermal Mn input at this site, leads to variable Mo/Mn ratios within the shallow oxic zone. Lower bottom water oxygen levels and a shallower oxidation front lead to enhanced plume U supply to the

seafloor during glacial periods. Glacial termination is inferred to be associated with a pulse of carbon supply to the seafloor that shallows the oxidation front further [*Martinez and Robinson*, 2010]. Subsequent deepening of the oxidation front during interglacial periods leads to oxygen burn down and relocation of the plume-derived U below the oxidation front.

Figure 8: Comparison of U/Fe and P/Fe ratios downcore from (a) 10^{o}S [*Schaller et al.*, 2000] and (b) the present study. High precision organic carbon data for the 10^{o}S site are plotted (dashed line). Shading indicates glacial periods for the 15^{o}S core determined from the age model (Fig. 2a).

References

Aller, R. C., and P. D. Rude, Complete oxidation of solid-phase sulfides by manganese and bacteria in anoxic marine sediments, *Geochimica et Cosmochimica Acta*, 52, 751-765, 1988.

Anderson, R. F., M. Q. Fleisher, Y. Lao, and G. Winckler, Modern $CaCO_3$ preservation in equatorial Pacific sediments in the context of late-Pleistocene glacial cycles, *Marine Chemistry*, 111, 30-46, 2008.

Bender, M., W. Broecker, V. Gornitz, U. Middel, R. Kay, S.-S. Sun, and P. Biscaye, Geochemistry of three cores from the East Pacific Rise, *Earth and Planetary Science Letters*, 12, 425-433, 1971.

Boyle, E. A., Vertical oceanic nutrient fractionation and glacial/interglacial CO_2 cycle, *Nature*, 331, 55-56, 1988.

Boyle, E. A., Cadmium and $\delta^{13}C$ paleochemical ocean distribution during the stage 2 glacial maximum, *Annu. Rev. Earth Planet. Sci.,* **20,** 245–287, 1992.

Broecker, W. S., and G. H. Denton, The role of ocean-atmosphere reorganizations in glacial cycles, *Geochimica et Cosmochimica Acta*, 53, 2465-2501, 1989.

Chen, J. H., R. L. Edwards, and G. J. Wasserburg, U-238,U-234 and Th-232 in seawater, *Earth and Planetary Science Letters*, 80, 241-251, 1986.

Colley, S., and J. Thomson, Recurrent uranium relocations in distal turbidites emplaced in pelagic conditions, *Geochimica Et Cosmochimica Acta*, 49, 2339-2348, 1985.

Dunk, R. M., and R. A. Mills, The impact of oxic alteration on plume-derived transition metals in ridge flank sediments from the East Pacific Rise, *Marine Geology*, 229, 133-157, 2006.

Dymond, J., Geochemistry of Nazca Plate surface sediments - an evaluation of hydrothermal, biogenic, detrital and hydrogenous sources, *Geological Society of America Memoir*, 154, 133-173, 1981.

Edmonds, H. N., and C. R. German, Particle geochemistry in the Rainbow hydrothermal plume, Mid-Atlantic Ridge, *Geochimica et Cosmochimica Acta*, 68, 759-772, 2004.

Feely, R. A., E. T. Baker, K. Marumo, T. Urabe, J. Ishibashi, J. Gendron, G. T. Lebon, and K. Okamura, Hydrothermal plume particles and dissolved phosphate over the superfast-spreading southern East Pacific Rise, *Geochimica et Cosmochimica Acta*, 60, 2297-2323, 1996.

Fiedler, P. C., and L. D. Talley, Hydrography of the eastern tropical Pacific: A review, *Progress in Oceanography*, 69, 143-180, 2006.

Fischer, J. P., T. G. Ferdelman, S. D'Hondt, H. Røy, and F. Wenzhofer, Oxygen penetration deep into the sediment of the South Pacific gyre, *Biogeosciences*, 6, 1467-1478, 2009.

Galbraith, E. D., S. L. Jaccard, T. F. Pedersen, D. M. Sigman, G. H. Haug, M. Cook, J. R. Southon and R. Francois, Carbon dioxide release from the North Pacific abyss during the last deglaciation, *Nature,* 449, 890–894, 2007.

German, C. R., S. Colley, M. R. Palmer, A. Khripounoff, and G. P. Klinkhammer, Hydrothermal plume-particle fluxes at 13 degrees N on the East Pacific Rise, *Deep-Sea Research Part I-Oceanographic Research Papers*, 49, 1921-1940, 2002.

Grevemeyer, I., B. Schramm, C. W. Devey, D. S. Wilson, B. Jochum, J. Hauschild, K. Aric, H. W. Villinger, and W. Weigel, A multibeam-sonar, magnetic and geochemical tow-line survey at 14o14'S on the southern East Pacific Rise - insights into the fourth dimension of ridge crest segmentation, *Earth and Planetary Science Letters*, 199, 359-372, 2002.

Hauschild, J., I. Grevemeyer, N. Kaul, and H. Villinger, Asymmetric sedimentation on young ocean floor at the East Pacific Rise, 15 degrees S, *Marine Geology*, 193, 49-59, 2003.

Heath, G. R., and J. Dymond, Metalliferous-sediment deposition in time and space – East Pacific Rise and Bauer Basin, Northern Nazca Plate, *Geological Society of America Memoirs*, 154, 175-197, 1981.

Imbrie, J., J. D. Hays, D. G. Martinson, A. McIntyre, A. C. Mix, J. J. Morley, N. G. Pisias, W. L. Prell, and N. J. Shackleton, The orbital forcing theory of Pleistocene climate: Support for a revised chronology of the marine ^{18}O isotope record. in *Milankovitch and Climate Part 1*, edited by Berger, A., J. Imbrie, J. Hays, G. Kukla and B. Saltzman, pp. 269-305, D Reidel Publishing Company, 1984.

Jaccard, S. L., E. D. Galbraith, D. M. Sigman, G. H. Huag, R. Francois, and T. F. Pedersen, Subarctic Pacific evidence for a glacial deepening of the oceanic respired carbon pool, *Earth and Planetary Science Letters*, 277, 156-165, 2009.

Lupton, J.E., and H. Craig, A Major He-3 Source at 15-Degrees-S on the East Pacific Rise, *Science,* 214, 13-18, 1981.

Marchig, V., J. Erzinger, and P. M. Heinze, Sediment in the black smoker area of the East Pacific Rise (18.5 Degrees-S), *Earth and Planetary Science Letters*, 79, 93-106, 1986.

Martinez, P., and R. S. Robinson, Increase in water column denitrification during the last deglaciation: the influence of oxygen demand in the eastern equatorial Pacific, *Biogeosciences*, 7, 1-9, 2010.

Matsumoto, K., T. Oba, J. Lynch-Stieglitz, and H. Yamamoto, Interior hydrography and circulation of the glacial Pacific Ocean, *Quaternary Science Reviews*, 21, 1693-1704, 2002.

McManus, J., W. M. Berelson, G. P. Klinkhammer, D. E. Hammond, and C. Holm, Authigenic uranium: relationship to oxygen penetration depth and organic carbon rain, *Geochimica et Cosmochimica Acta*, 69, 95-108, 2005.

Metz, S., and J. H. Trefry, Field and laboratory studies of metal uptake and release by hydrothermal precipitates, *Journal of Geophysical Research-Solid Earth*, 98, 9661-9666, 1993.

Mills, R. A., and H. Elderfield, Hydrothermal activity and the geochemistry of metalliferous sediment, *AGU Monograph*, 92, 391-407, 1995.

Mills, R. A., J. Thomson, H. Elderfield, R. W. Hinton, and E. Hyslop, Uranium enrichment in metalliferous sediments from the Mid-Atlantic Ridge, *Earth and Planetary Science Letters*, 124, 35-47, 1994.

Mills, R. A., and R. M. Dunk, Tracing low-temperature fluid flow on ridge flanks with sedimentary uranium distribution, Geochem. Geophys. Geosyst., 11, Q08009, doi:10.1029/2010GC003157, 2010.

Morford, J. L., S. R. Emerson, E. J. Breckel, and S. H. Kim, Diagenesis of oxyanions (V, U, Re, and Mo) in pore waters and sediments from a continental margin, *Geochimica et Cosmochimica Acta*, 69, 5021-5032, 2005.

Murray, R. W., C. Knowlton, M. Leinen, A. C. Mix, and C. H. Polsky, Export production and carbonate dissolution in the central Equatorial Pacific Ocean over the past 1 Myr, *Paleoceanography*, 15, 570–592, 2000.

Okazaki, Y., A. Timmermann, L. Menviel, N. Harada, A. Abe-Ouchi, M.O. Chikamoto, A. Mouchet and H. Asahi, Deepwater formation in the North Pacific during the last glacial termination, *Science*, 329, 200-204, 2010.

Paillard, D., L. Labeyrie, and P. Yiou, Macintosh programme performs time series analysis., *EOS, Trans. Amer. Geophys. U.*, 77, 379, 1996.

Poulton, S. W., and D. E. Canfield, Co-diagenesis of iron and phosphorus in hydrothermal sediments from the southern East Pacific Rise: Implications for the evaluation of paleoseawater phosphate concentrations, *Geochimica et Cosmochimica Acta*, 70, 5883-5898, 2006.

Reid, J. L., Evidence of an effect of heat-flux from the East Pacific Rise upon the characteristics of the mid-depth waters, *Geophysical Research Letters*, 9, 381-384, 1982.

Rydell, H., T. Kraemer, K. Bostrom, and O. Joensuu, Postdepositional injections of uranium-rich solutions into East Pacific Rise sediments, *Marine Geology*, 17, 151-164, 1974.

Schaller, T., J. Morford, S. R. Emerson, and R. A. Feely, Oxyanions in metalliferous sediments: Tracers for paleoseawater metal concentrations?, *Geochimica et Cosmochimica Acta*, 64, 2243-2254, 2000.

Schippers, A., and B. B. Jørgensen, Oxidation of pyrite and iron sulfide by manganese dioxide in marine sediments, *Geochimica et Cosmochimica Acta*, 65, 915-922, 2001.

Schramm, B., C. W. Devey, K. M. Gillis, and K. Lackschewitz, Quantitative assessment of chemical and mineralogical changes due to progressive low-temperature alteration of East Pacific Rise basalts from 0 to 9 Ma, *Chemical Geology*, 218, 281-313, 2005.

Shackleton, N. J., A. Berger, and W. R. Peltier, An alternative astronomical calibration of the lower Pleistocene time scale based on ODP site 677, *Trans. R. Soc. Edinburgh: Earth Sci.*, 81, 251-261, 1990.

Shackleton, N. J., and M. A. Hall, Stable isotope records in bulk sediments (Leg 138). in *Proc. ODP, Sci. Results*, edited by Pisias, N. G., L. A. Mayer, T. R. Janecek, A. Palmer-

Julson and T. H. van Andel, pp. 797–805, Ocean Drilling Program, College Station, TX, 1995.

Shimmield, G. B., and N. B. Price, The behavior of molybdenum and manganese during early sediment diagenesis - offshore Baja-California, Mexico, *Marine Chemistry*, 19, 261-280, 1986.

Shimmield, G. B., and N. B. Price, The scavenging of U, Th-230 and Pa-231 during pulsed hydrothermal activity at 20-Degrees-S, East Pacific Rise, *Geochimica et Cosmochimica Acta*, 52, 669-677, 1988.

Sigman, D. M., and E. A. Boyle, Glacial/interglacial variations in atmospheric carbon dioxide, *Nature*, 407, 859-869, 2000.

Stott, L., J. Southon, A. Timmermann and A. Koutavas, Radiocarbon age anomaly at intermediate water depth in the Pacific Ocean during the last deglaciation, *Paleoceanography*, 24, PA2223, doi:10.1029/2008PA001690.

Thomson, J., N. C. Higgs, and S. Colley, Diagenetic redistributions of redox-sensitive elements in northeast Atlantic glacial/interglacial transition sediments, *Earth and Planetary Science Letters*, 139, 365-377, 1996.

Thomson, J., N. C. Higgs, I. Jarvis, D. J. Hydes, S. Colley, and T. R. S. Wilson, The behavior of manganese in Atlantic carbonate sediments, *Geochimica et Cosmochimica Acta*, 50, 1807-1818, 1986.

Trocine, R. P., and J. H. Trefry, Distribution and chemistry of suspended particles from an active hydrothermal vent site on the Mid-Atlantic Ridge at 26-degrees-N, *Earth and Planetary Science Letters*, 88, 1-15, 1988.

Veeh, H., and K. Boström, Anomalous $^{234}U/^{238}U$ on the East Pacific Rise, *Earth and Planetary Science Letters*, 10, 372-374, 1971.

Venuti, A., F. Florindo, E. Michel, and I. R. Hall, Magnetic proxy for the deep (Pacific) western boundary current variability across the mid-Pleistocene climate transition, *Earth and Planetary Science Letters*, 259, 107-118, 2007.

Yang, Y. L., H. Elderfield, T. F. Pedersen, and M. Ivanovich, Geochemical record of the Panama Basin during the Last Glacial Maximum carbon event shows that the glacial ocean was not suboxic, *Geology*, 23, 1115-1118, 1995.

Depth (cm)	Age (ka)	Fe (%)	Mn (%)	Ca (%)	Al (ppm)	Si (%)	P (%)	U (ppm)
5.25	4.5	5.92	1.68	28.5	700	1.34	0.286	5.0
15.5	13.3	4.97	1.50	29.7	738	1.29	0.292	7.1
20.5	18.3	5.84	1.65	28.1	670	1.33	0.314	6.7
25.5	22.8	4.69	1.71	29.6	733	1.14	0.244	4.8
30.5	27.3	5.74	2.06	28.6	830	1.37	0.324	5.0
35.5	31.8	6.33	2.31	27.7	801	1.47	0.407	8.2
40.5	36.3	5.30	1.96	28.6	691	1.26	0.347	8.5
45.5	40.8	4.89	1.78	29.5	742	1.22	0.286	8.2
50.5	45.3	4.96	1.78	29.9	746	1.23	0.287	8.3
55.5	49.8	5.14	1.81	29.7	763	1.30	0.311	8.1
60.5	54.4	5.69	1.97	28.6	792	1.47	0.372	8.3
65.5	58.9	6.15	2.14	28.0	704	1.38	0.403	8.2
70.5	63.4	6.04	2.26	28.2	717	1.35	0.375	7.4
75.5	67.9	5.96	2.21	28.7	771	1.35	0.343	7.3
80.5	72.4	5.83	2.07	28.8	830	1.31	0.307	4.7
85.5	76.9	6.04	2.13	28.4	851	1.34	0.289	4.9
90.5	81.4	5.99	2.16	28.7	818	1.30	0.260	3.7
95.5	85.9	6.37	2.43	27.8	805	1.37	0.282	5.7
100.5	90.4	5.88	2.27	28.8	729	1.25	0.261	5.0
115.5	103.9	6.01	2.18	28.6	746	1.31	0.281	5.2
120.5	108.4	6.76	2.54	27.5	822	1.38	0.286	5.4
125.5	113	6.17	2.34	28.2	860	1.30	0.258	4.1
135.5	121.9	5.88	2.12	28.6	969	1.28	0.241	3.6
138	123.9	5.59	1.99	29.0	910	1.19	0.222	4.0
140.5	126	5.78	1.92	29.0	914	1.21	0.222	4.0
143	128	5.69	1.93	29.1	885	1.20	0.224	6.0
145.5	130	6.13	1.95	28.5	927	1.34	0.262	3.5
148	132.1	6.72	2.10	28.3	897	1.27	0.279	8.3
153	136.1	6.42	2.07	27.9	872	1.35	0.337	8.6
155.5	138.2	5.53	1.88	29.1	801	1.27	0.325	8.3
158	140.2	5.62	1.96	30.0	834	1.17	0.304	11.3
160.5	142.2	5.10	1.87	29.5	797	1.23	0.331	8.6
163	144.3	5.59	2.01	28.5	855	1.32	0.386	12.6
165.5	146.3	5.95	2.14	28.1	784	1.39	0.466	11.3
168	148.3	6.25	2.14	27.6	738	1.39	0.501	12.6
178	156.5	5.91	2.21	28.0	717	1.34	0.463	11.9
188	164.6	4.98	1.99	29.5	754	1.18	0.294	8.2
193	168.7	5.05	1.96	30.4	733	1.06	0.241	6.9
198	172.7	4.91	2.04	29.7	746	1.14	0.247	5.6
203	176.8	4.89	2.06	29.7	742	1.12	0.231	5.7
208	180.9	5.23	2.18	30.0	834	1.20	0.263	4.3
213	184.9	5.08	2.06	29.4	733	1.17	0.278	4.8
223	191	5.70	2.20	29.5	746	1.11	0.272	6.1
228	194.1	5.49	2.15	30.1	729	1.04	0.226	4.7
233	197.1	6.14	2.48	28.8	965	1.35	0.275	4.3
238	200.2	6.47	2.72	28.3	897	1.37	0.299	4.3
243	203.3	5.85	2.37	29.5	750	1.09	0.236	4.5
248	206.3	6.32	2.53	28.8	944	1.26	0.273	5.8
253	209.4	5.71	2.32	29.6	960	1.14	0.233	3.6
258	212.4	5.62	2.31	29.4	1032	1.21	0.237	4.3
263	215.5	5.63	2.34	29.8	805	1.12	0.243	4.3
268	218.5	5.87	2.80	28.6	906	1.34	0.333	5.3
273	221.6	5.79	2.52	29.1	733	1.12	0.312	6.3

278	224.6	6.12	2.62	29.1	691	1.11	0.310	5.7
283	227.7	5.39	2.48	29.8	754	1.13	0.246	3.5
288	230.7	5.87	2.99	29.5	712	1.05	0.216	4.3
293	233.8	6.66	2.44	28.8	633	1.15	0.263	3.5
298	236.8	7.38	2.57	28.0	574	1.24	0.324	6.0
303	239.9	7.71	2.69	27.6	624	1.33	0.324	8.0
308	242.9	4.43	1.55	31.7	591	0.92	0.211	8.1
313	246	4.64	1.75	30.7	775	1.19	0.287	11.3
318	249	4.40	1.60	30.5	662	1.07	0.231	7.5
333	258.2	4.27	1.63	30.5	696	1.13	0.296	9.9
338	261.2	4.66	1.82	30.7	754	1.23	0.335	9.7
343	264.3	5.13	1.97	29.9	771	1.32	0.414	11.9
348	267.3	6.08	2.34	28.5	792	1.44	0.484	14.8
353	270.4	6.65	2.58	27.9	855	1.47	0.457	12.2
358	273.4	6.83	2.66	27.9	897	1.49	0.409	9.3
363	276.5	7.19	2.81	27.3	902	1.51	0.423	10.2
373	282.6	6.46	2.69	28.2	725	1.39	0.374	8.4
378	285.6	5.78	2.29	29.6	582	1.09	0.316	8.0
383	288.7	5.74	2.30	29.4	662	1.24	0.349	6.6
388	291.7	5.87	2.51	29.1	691	1.24	0.317	6.6
393	294.8	5.88	2.62	29.0	717	1.23	0.292	7.6
398	297.8	5.78	2.59	29.2	763	1.25	0.280	6.8
403	300.9	5.60	2.34	28.8	721	1.24	0.293	6.6
408	303.9	5.68	2.41	28.4	675	1.25	0.339	8.3
413	307	6.07	2.56	28.8	679	1.31	0.371	7.8
418	310	6.42	2.39	28.6	889	1.36	0.336	6.2
423	313.1	6.65	2.56	28.3	729	1.41	0.377	8.6
428	316.1	6.08	2.26	29.3	775	1.31	0.314	6.2
433	319.2	5.52	2.06	29.9	628	1.06	0.220	4.0
438	322.2	5.69	2.39	29.3	683	1.23	0.250	3.8
443	325.3	5.85	2.26	29.7	553	1.09	0.246	5.8
448	328.3	6.76	2.06	29.1	507	1.16	0.319	6.3
453	331.4	7.67	2.45	26.1	599	1.54	0.431	7.0
458	334.4	6.35	2.07	28.0	607	1.30	0.358	6.4
463	337.5	5.81	2.05	28.6	662	1.26		3.8
468	340.5	5.55	1.95	29.0	649	1.20	0.309	5.5
473	343.6	5.30	2.06	29.9	687	1.16	0.331	6.6
478	346.7	5.17	2.02	29.9	708	1.19	0.338	7.6
483	349.7	5.48	2.21	28.7	645	1.21	0.388	10.4
488	352.8	5.85	2.17	28.1	679	1.29	0.476	14.3
498	358.9	5.31	1.93	30.4	696	1.07	0.328	12.9
503	362	5.83	2.08	29.7	712	1.15	0.365	14.8
508	365.1	6.53	2.45	28.6	729	1.23	0.391	14.7
513	368.1	6.67	2.69	26.5	771	1.38	0.402	12.1
518	371.2	6.47	2.85	27.2	763	1.37	0.377	10.7
523	374.3	6.66	2.76	27.9	843	1.41	0.343	9.7
528	377.3	6.37	2.60	28.1	834	1.37	0.328	10.9
533	380.4	6.47	2.66	27.6	780	1.36	0.302	7.9
538	383.5	6.92	2.83	27.7	826	1.41	0.310	11.4
543	386.5	6.62	2.88	27.4	775	1.35	0.251	7.3
548	389.6	8.81	3.89	24.2	780	1.65	0.279	7.6
553	392.7	8.50	3.62	24.9	830	1.61	0.273	8.2
558	395.7	7.93	3.53	24.7	708	1.49	0.251	8.5
568	401.9	5.42	2.39	29.8	725	1.18	0.214	6.9
573	404.9	5.18	2.10	30.0	540	0.96	0.196	5.7

578	408	6.03	2.17	29.8	612	1.07	0.231	8.5
603	423.8	5.56	2.16	28.6	637	1.25	0.425	13.3
613	430.1	4.67	1.86	30.0	641	1.10	0.286	9.4
623	436.5	5.74	2.32	28.7	662	1.29	0.397	16.8
628	439.6	6.25	2.61	27.6	637	1.42	0.538	27.9
633	442.8	6.42	2.55	28.0	700	1.48	0.505	30.3
638	445.9	5.64	2.29	28.2	637	1.32	0.453	26.2
648	452.3	5.32	2.07	29.4	557	1.05	0.335	14.1
653	455.4	5.20	2.12	29.4	645	1.17	0.376	13.4
658	458.6	5.41	2.24	29.0	675	1.18	0.364	12.5
663	461.7	5.95	2.41	28.0	725	1.28	0.404	17.0
668	464.9	6.77	2.90	27.1	788	1.37	0.345	14.0
673	468.1	7.60	3.61	25.5	839	1.53	0.346	15.6
683	474.4	8.55	3.49	24.7	826	1.70	0.388	18.5
688	477.6	7.84	3.06	26.0	809	1.58	0.296	9.9
693	482.5	7.48	2.88	26.6	750	1.50	0.284	11.4
698	487.7	7.92	3.05	25.9	712	1.54	0.319	13.7
703	493	8.40	3.28	25.3	721	1.62	0.361	14.7
708	498.3	7.59	3.10	26.2	717	1.52	0.325	12.4
713	503.6	7.31	2.82	26.7	754	1.49	0.297	10.7
718	508.8	7.58	2.93	26.4	729	1.47	0.305	12.3
723	514.1	8.06	3.11	25.9	733	1.55	0.343	12.9
728	519.4	8.85	3.41	24.6	733	1.74	0.446	17.3
733	524.7	7.64	2.96	26.1	687	1.53	0.425	16.1
738	529.9	6.78	2.64	27.1	704	1.45	0.402	15.2
743	535.2	6.45	2.59	27.6	704	1.39	0.386	14.6
748	540.5	6.49	2.64	27.5	696	1.37	0.402	13.3
753	545.8	6.92	2.91	26.7	746	1.47	0.434	14.0
758	551	6.45	2.74	27.2	759	1.41	0.412	13.6
763	556.3	6.26	2.57	27.7	813	1.37	0.356	10.5
768	561.6	6.72	2.76	27.0	792	1.42	0.395	13.1
773	566.9	7.45	3.12	26.0	767	1.51	0.417	16.0
778	571.7	7.89	3.59	25.6	784	1.54	0.360	14.0
783	575.6	7.38	3.37	26.3	830	1.47	0.305	11.9
793	583.3	7.32	3.44	26.0	729	1.50	0.401	16.6
798	587.2	7.10	3.09	26.3	708	1.45	0.449	14.0
803	591.1	6.59	2.87	27.3	725	1.36	0.368	11.8
808	595	6.69	3.00	27.0	763	1.43	0.362	15.5
813	598.9	7.04	2.89	26.7	830	1.47	0.348	14.3
818	602.8	7.26	2.89	26.7	759	1.48	0.318	11.9
823	606.6	7.40	2.96	26.6	754	1.44	0.273	10.8
828	610.5	7.42	2.93	26.6	792	1.49	0.276	10.4
833	614.4	8.96	3.45	24.6	830	1.74	0.352	14.3
838	618.3	10.44	4.03	22.5	733	1.96	0.540	18.8
843	622.2	8.78	4.65	23.8	687	1.68	0.463	15.6
848	626.1	6.90	4.57	26.0	679	1.43	0.396	11.2
853	630	6.35	2.39	27.8	662	1.33	0.411	10.1
858	634.2	6.49	2.51	27.6	670	1.37	0.450	11.4
863	638.5	6.19	2.35	28.0	754	1.36	0.435	9.0
868	642.7	6.41	2.50	27.7	704	1.34	0.437	11.4
873	647	7.75	6.24	23.9	742	1.58	0.493	14.8
878	651.2	8.49	3.06	24.9	717	1.67	0.569	12.9
883	655.5	7.82	3.14	25.7	754	1.61	0.488	11.1
888	659.7	7.08	2.70	26.9	704	1.39	0.436	9.2
893	664	6.84	2.46	27.3	767	1.39	0.372	8.6

898	668.2	7.18	2.58	27.0	788	1.42	0.362	7.9
903	672.5	9.08	3.34	24.6	805	1.70	0.451	10.5
908	676.7	8.33	3.24	25.4	881	1.62	0.342	9.5
913	681	9.11	3.53	24.5	864	1.63	0.321	10.5
918	685.2	10.38	3.95	22.7	822	1.92	0.477	12.7
923	689.5	8.22	3.53	25.3	822	1.62	0.338	11.0
928	693.7	8.18	3.12	25.6	805	1.62	0.336	8.9
933	698	7.42	3.02	26.4	847	1.52	0.319	10.7
938	702.2	7.43	3.21	26.2	872	1.56	0.356	11.1
943	706.5	7.57	3.19	25.6	1078	1.73	0.471	17.5
948	710.7	6.66	2.77	26.6	1162	1.63	0.432	11.6
953	715	7.19	3.06	26.0	1007	1.61	0.480	10.0
958	719.2	7.00	3.33	26.2	923	1.53	0.447	8.6
963	723.5	7.52	2.72	26.2	1091	1.70	0.500	9.9
968	727.7	6.69	2.84	27.0	1082	1.58	0.393	8.4
973	732	6.58	4.07	26.5	927	1.50	0.337	10.3
978	736.3	7.47	3.42	25.8	893	1.69	0.403	9.7
983	740.5	7.92	3.94	25.0	868	1.76	0.457	8.8

Data gaps indicate measurement below detection limit

Mo (ppm)	Cd (ppm)	V (ppm)	Cu (ppm)	Ba (ppm)
8.6	11.8	178	245	1294
7.0	18.4	140	173	1101
8.5	16	169	237	1222
10.5	10.4	134	165	1261
15.0	17.6	184	211	1361
19.2	22.5	209	244	1319
15.8	18.4	164	200	1210
10.8	30.6	150	174	1189
11.7	22.8	146	178	1154
11.2	17.9	157	182	1284
14.2	16.4	182	204	1294
19.2	21.1	191	239	1287
21.7	20.9	203	237	1397
21.7	30.5	195	236	1478
19.7	14.4	195	225	1497
22.8	18.7	208	237	1626
24.1	19	207	251	1702
29.7	15.4	230	283	1764
30.8	16.2	200	269	1508
28.1	20.3	198	264	1465
39.0	37.7	246	323	1837
40.5	21	220	294	1812
33.9	24.1	205	264	1667
32.5	20.3	183	252	1520
23.7	21.6	188	248	1442
19.6	6.0	184	250	1288
17.4	22.1	206	243	1403
21.7	9.2	218	303	1105
14.1	18.4	209	247	1165
7.1	13.2	172	196	1105
18.5		170	224	1283
6.2	27	150	180	1165
7.9	20.9	174	197	1231
7.3	20.1	190	208	1283
7.9	20.9	190	228	1231
5.7	22.1	192	213	1274
4.6	16.1	161	178	1334
3.8	22.8	148	204	1357
4.5	16.4	160	183	1385
3.6	15.2	154	186	1355
4.6	22.8	175	224	1498
2.7	18.1	165	199	1398
4.3	18.5	187	260	1474
4.2	25.5	178	261	1541
5.1	26.4	218	302	1773
6.5	33.7	236	334	1720
5.4	3.1	197	302	1375
4.3	23.9	221	326	1460
4.5	21.1	191	292	1287
4.4	22.2	186	282	1388
4.5	13.8	185	280	1427
9.8	20.6	214	282	1520
7.2	10.2	191	265	1343

8.1	18.5	219	280	1376
7.4	32.9	197	249	1373
15.5	19.2	214	296	1486
5.3	6.8	237	327	1331
4.6	16.7	265	370	1285
4.9	16.9	274	380	1318
	12.9	122	176	944
	28.2	136	187	1106
	21.0	134	157	1055
	26.3	124	154	1123
	18.9	143	189	1120
	20.5	162	211	1235
1.8	24.1	198	259	1307
1.4	26.4	220	295	1458
2.3	23.8	237	309	1534
2.2	38.9	248	333	1617
2.4	27.7	230	309	1456
2.2	18.7	184	272	1182
2.3	26.6	196	262	1230
2.2	20.3	206	275	1318
3.5	9.3	210	281	1377
5.0	11.2	210	276	1383
1.5	20.4	197	237	1351
3.4	25.0	201	251	1332
3.1	21.0	221	287	1296
2.1	16.5	233	291	1421
2.4	25.7	243	307	1381
2.0	31.0	217	271	1400
2.5	19.9	180	257	1197
5.3	21.0	201	268	1268
4.9	37.5	195	279	1160
1.9	21.6	217	314	922
	25.4	287	329	1124
1.5	20.5	225	262	874
	16.1	209	221	916
	24.8	194	203	946
1.6	21.4	177	211	1002
1.2	31.4	174	207	1039
	9.0	180	203	998
	18.2	189	217	1020
	14.1	158	226	989
	8.3	176	253	1119
1.7	36.7	203	297	1250
1.4	22.6	221	282	1374
2.3	32.0	224	284	1401
2.0	24.7	231	315	1426
1.9	11.9	217	303	1373
1.6	19.5	228	293	1453
2.5	23.4	248	347	1462
1.8	22.8	249	323	1533
4.4	26.6	343	477	1816
2.5	24.6	325	447	1792
3.0	30.6	304	412	1622
2.5	10.3	191	263	1288
	21.4	174	220	1092

	23.7	197	271	1070
	10.6	180	198	1011
	21.1	145	167	906
	10.5	191	215	1018
	10.7	210	238	1120
	20.2	223	262	1142
	18.6	179	211	990
	22.1	166	212	942
	20.5	164	202	957
1.1	20.9	175	214	1070
	19.5	199	244	1139
1.8	16.4	233	334	1233
4.3	21.4	284	367	1537
2.2	20.3	327	408	1505
	13.0	299	372	1274
1.8	26.0	288	359	1179
	16.6	302	384	1197
2.7	24.3	332	416	1309
1.0	12.9	302	364	1203
	24.5	287	331	1076
1.4	17.3	297	341	1113
	17.3	320	368	1190
1.8	21.4	352	420	1309
1.5	9.2	293	346	1169
1.0	14.0	247	289	1087
	19.3	236	266	1100
1.1	27.5	230	269	1101
	25.3	259	287	1288
	24.7	238	270	1220
	24.5	230	264	1226
1.4	17.7	243	296	1308
1.1	27.0	279	348	1448
3.8	23.0	319	403	1517
3.6	29.7	288	376	1516
5.7	18.0	286	370	1463
4.0	15.8	267	321	1290
2.4	17.6	243	294	1379
4.1	23.4	246	308	1329
2.1	25.1	259	321	1488
1.6	24.8	274	336	1465
1.1	26.0	296	355	1491
1.4	36.5	285	354	1435
2.3	21.0	352	453	1465
3.9	28.5	420	538	1435
13.1	27.8	360	415	1461
16.8	22.6	269	304	1303
	12.5	223	210	947
1.0	29.2	231	220	985
	28.7	214	205	1019
2.3	17.8	221	210	1067
30.8	29.4	327	363	1596
3.3	22.4	313	310	1157
3.0	22.0	293	298	1260
2.2	27.1	253	269	1181
1.5	19.8	245	261	1215

1.3	26.2	270	286	1340
3.4	24.7	368	408	1481
2.6	24.3	344	392	1575
3.2	26.2	374	457	1640
4.1	25.8	441	548	1569
5.2	10.0	341	419	1367
1.8	23.0	340	392	1285
2.7	25.8	298	351	1266
2.5	21.3	285	344	1241
2.7	35.3	280	328	1202
2.0	25.0	228	270	1075
4.5	7.2	263	294	1073
6.3	15.9	266	298	1081
1.9	16.8	284	263	965
2.7	22.8	255	240	1076
13.8	23.3	275	296	1354
5.7	24.0	311	301	1215
9.7	21	341	353	1378

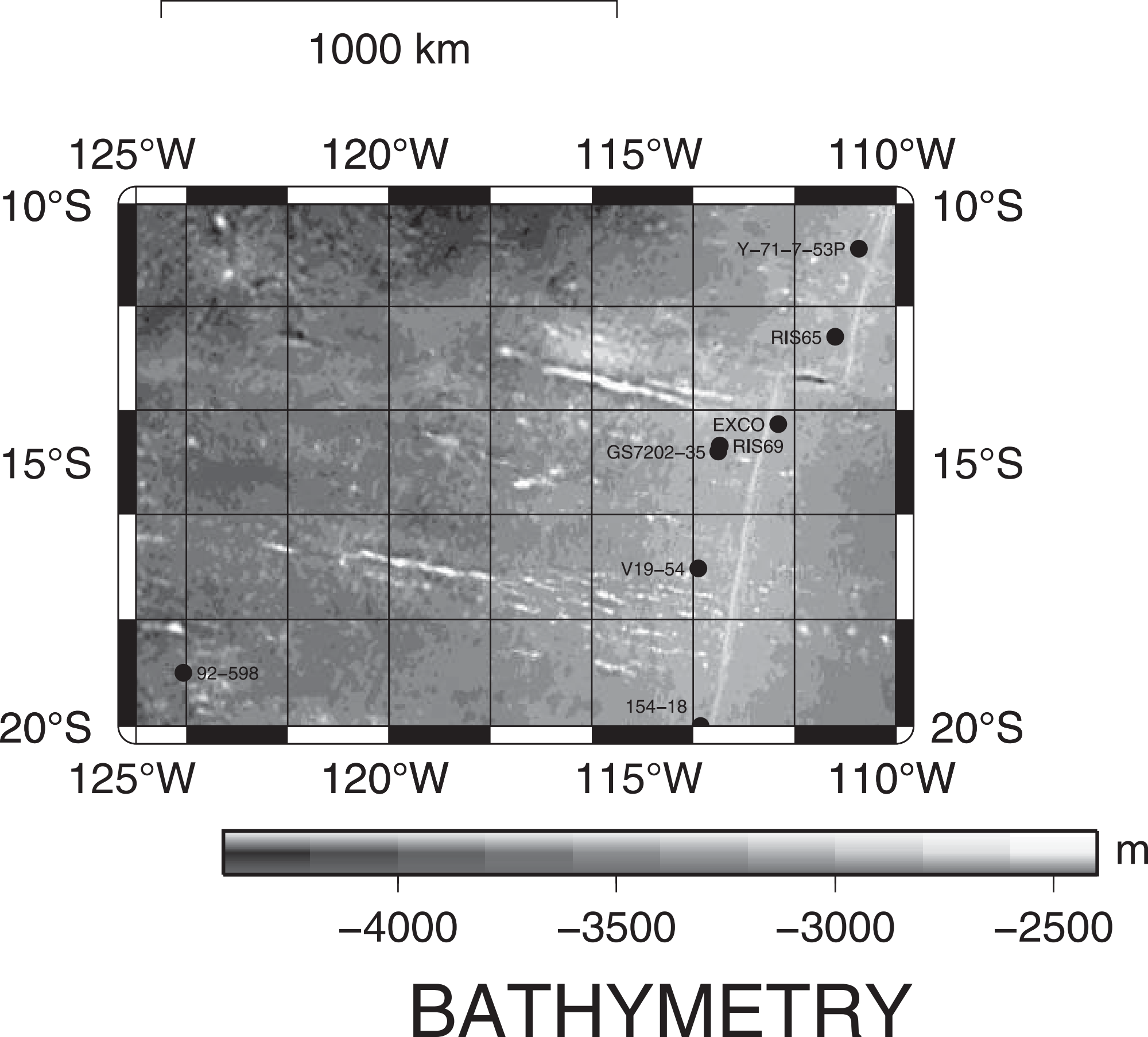
1000 km
125°W
120°W
115°W
110°W
10°S
15°S
20°S
Y–71–7–53P
RIS65
EXCO
GS7202–35
RIS69
V19–54
92–598
154–18
m
–4000
–3500
–3000
–2500
BATHYMETRY

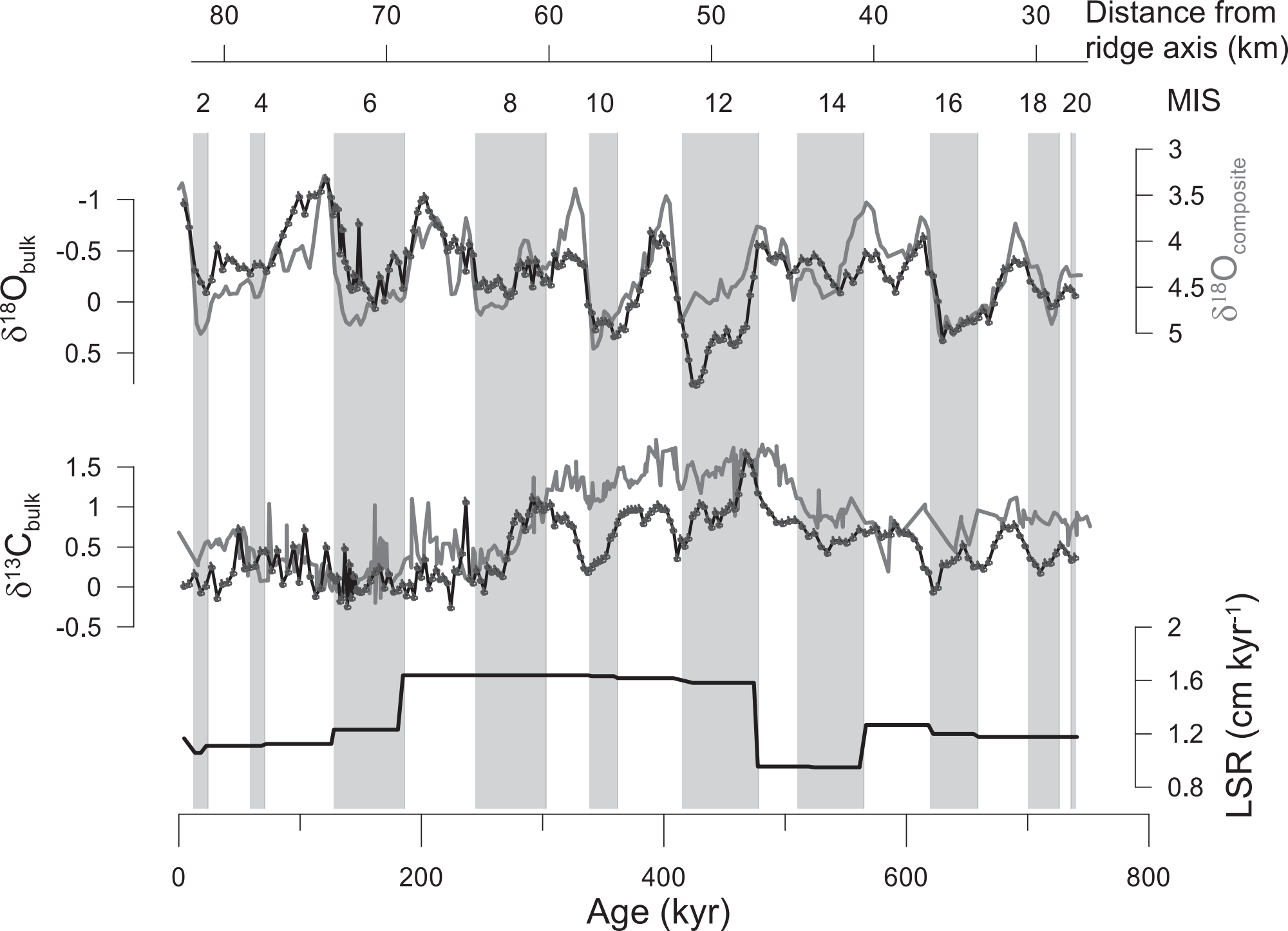
80
70
60
50
40
30
Distance from ridge axis (km)
2
4
6
8
10
12
14
16
18
20
MIS
-1
-0.5
0
0.5
δ18Obulk
3
3.5
4
4.5
5
δ18Ocomposite
1.5
1
0.5
0
-0.5
δ13Cbulk
2
1.6
1.2
0.8
LSR (cm kyr-1)
0
200
400
600
800
Age (kyr)

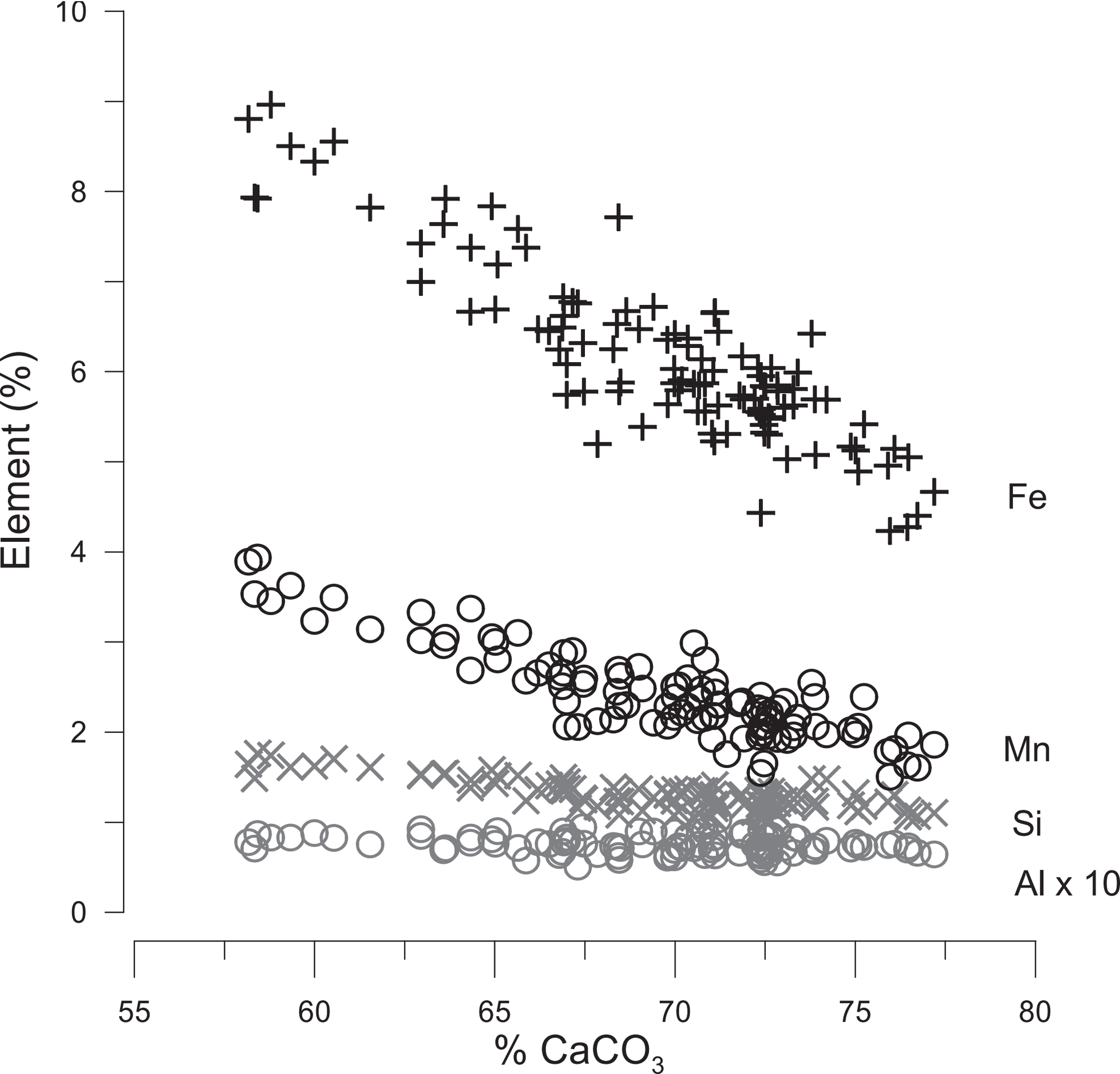
Element (%)
10
8
6
4
2
0
Fe
Mn
Si
Al x 10
55
60
65
70
75
80
% CaCO3

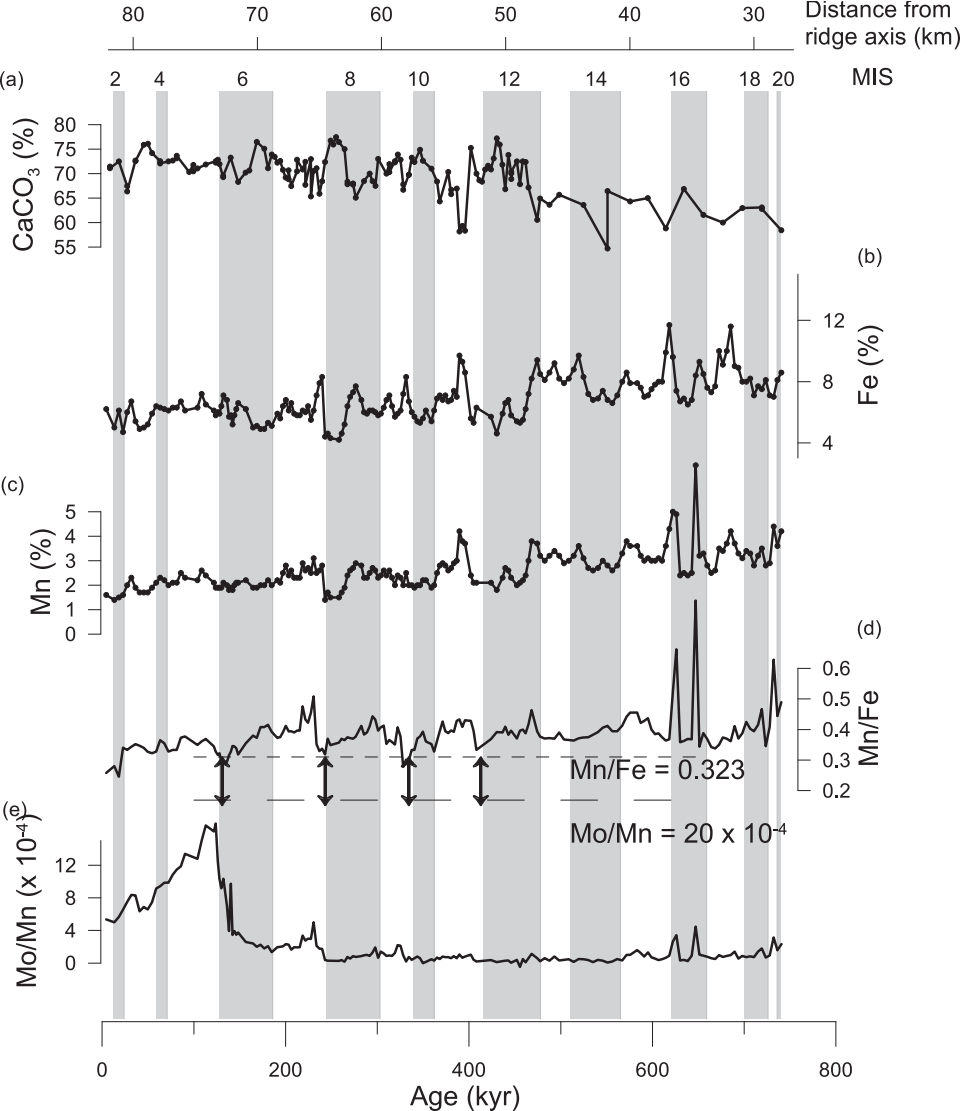
Distance from ridge axis (km)
80
70
60
50
40
30
(a)
2
4
6
8
10
12
14
16
18
20
MIS
CaCO3 (%)
80
75
70
65
60
55
(b)
Fe (%)
12
8
4
(c)
Mn (%)
5
4
3
2
1
0
(d)
Mn/Fe
0.6
0.5
0.4
0.3
0.2
Mn/Fe = 0.323
(e)
Mo/Mn (x 10-4)
Mo/Mn = 20 x 10-4
12
8
4
0
0
200
400
600
800
Age (kyr)

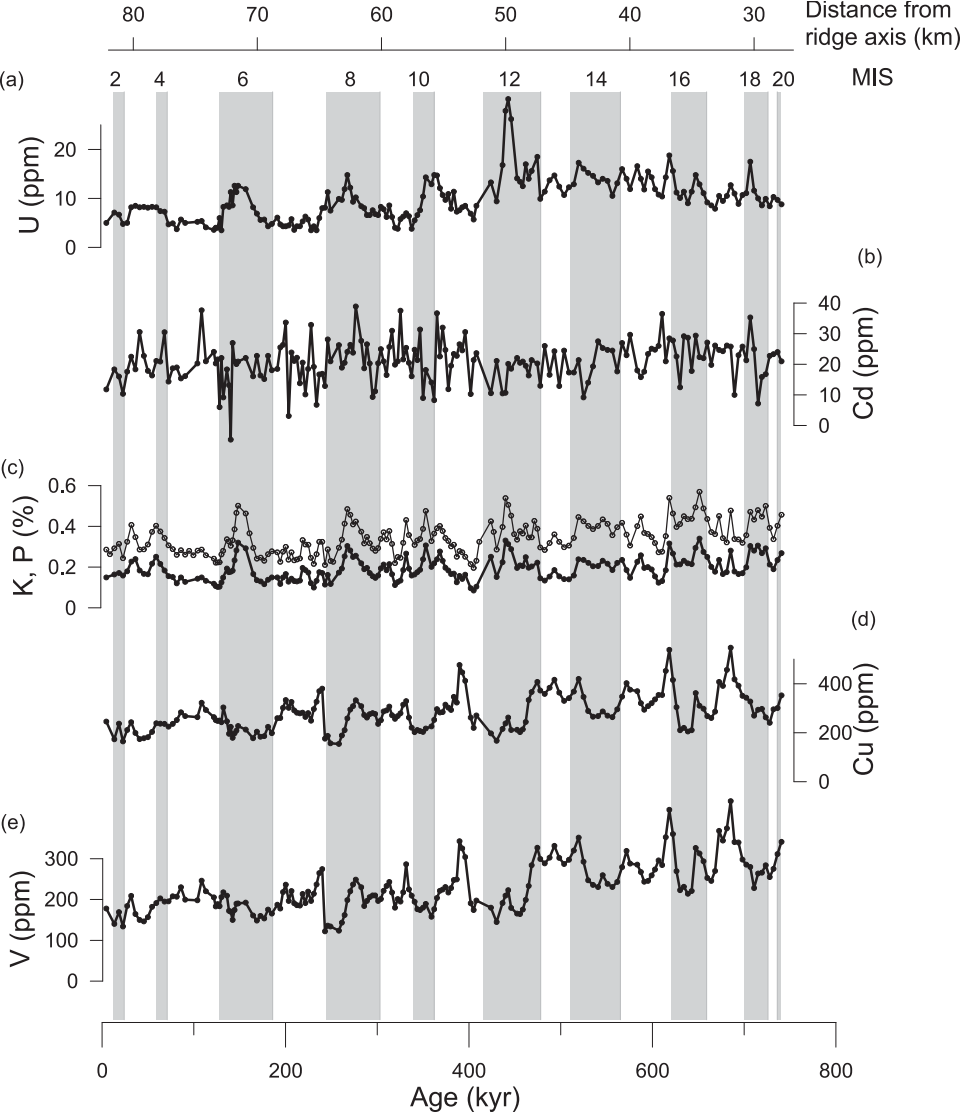
Distance from ridge axis (km)
80
70
60
50
40
30
(a)
2
4
6
8
10
12
14
16
18
20
MIS
U (ppm)
20
10
0
(b)
Cd (ppm)
40
30
20
10
0
(c)
K, P (%)
0.6
0.4
0.2
0
(d)
Cu (ppm)
400
200
0
(e)
V (ppm)
300
200
100
0
0
200
400
600
800
Age (kyr)

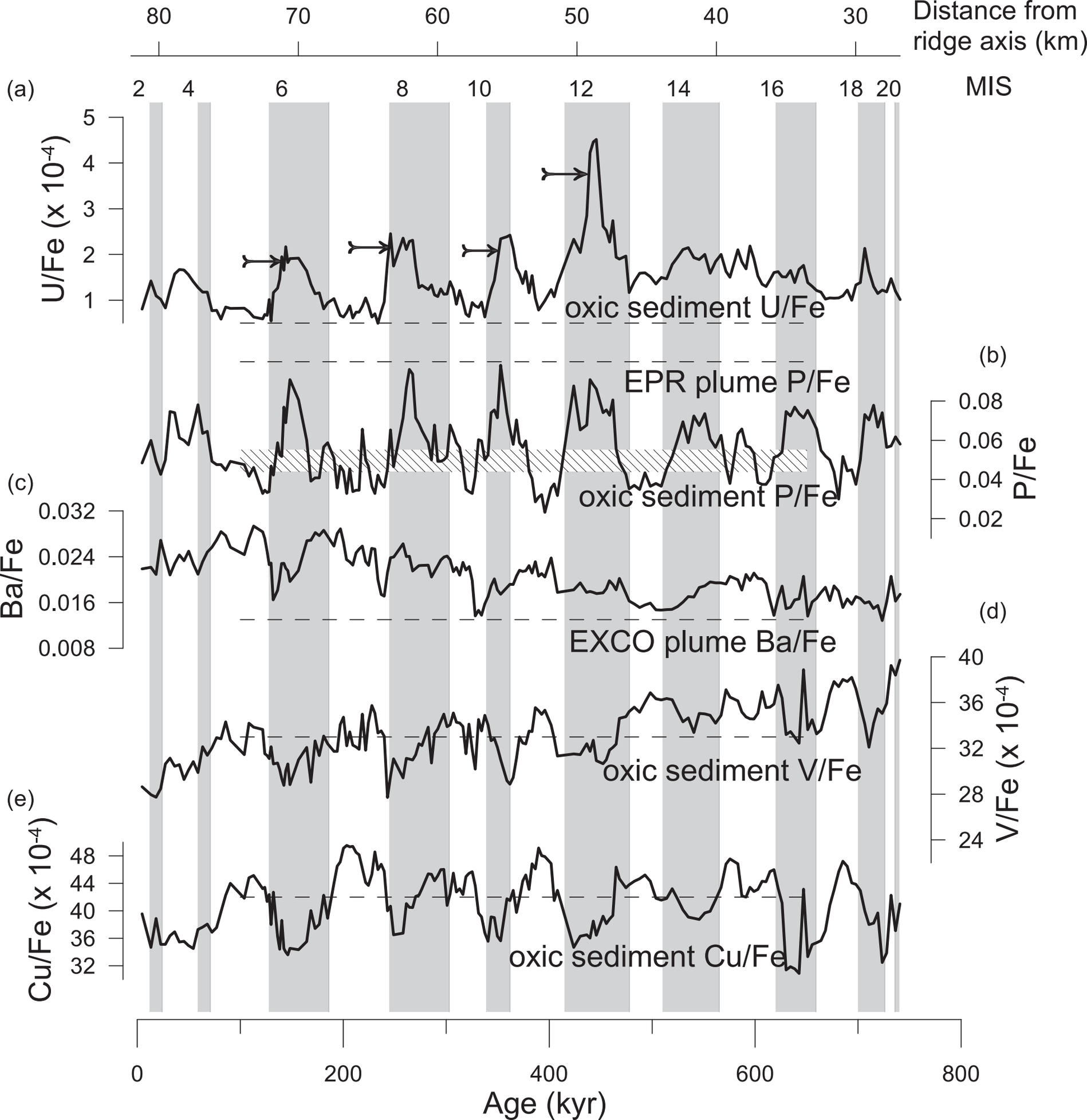
80
70
60
50
40
30
Distance from ridge axis (km)
(a)
2
4
6
8
10
12
14
16
18
20
MIS
U/Fe (x 10-4)
5
4
3
2
1
oxic sediment U/Fe
(b)
EPR plume P/Fe
oxic sediment P/Fe
0.08
0.06
0.04
0.02
P/Fe
(c)
Ba/Fe
0.032
0.024
0.016
0.008
EXCO plume Ba/Fe
(d)
oxic sediment V/Fe
40
36
32
28
24
V/Fe (x 10-4)
(e)
Cu/Fe (x 10-4)
48
44
40
36
32
oxic sediment Cu/Fe
0
200
400
600
800
Age (kyr)

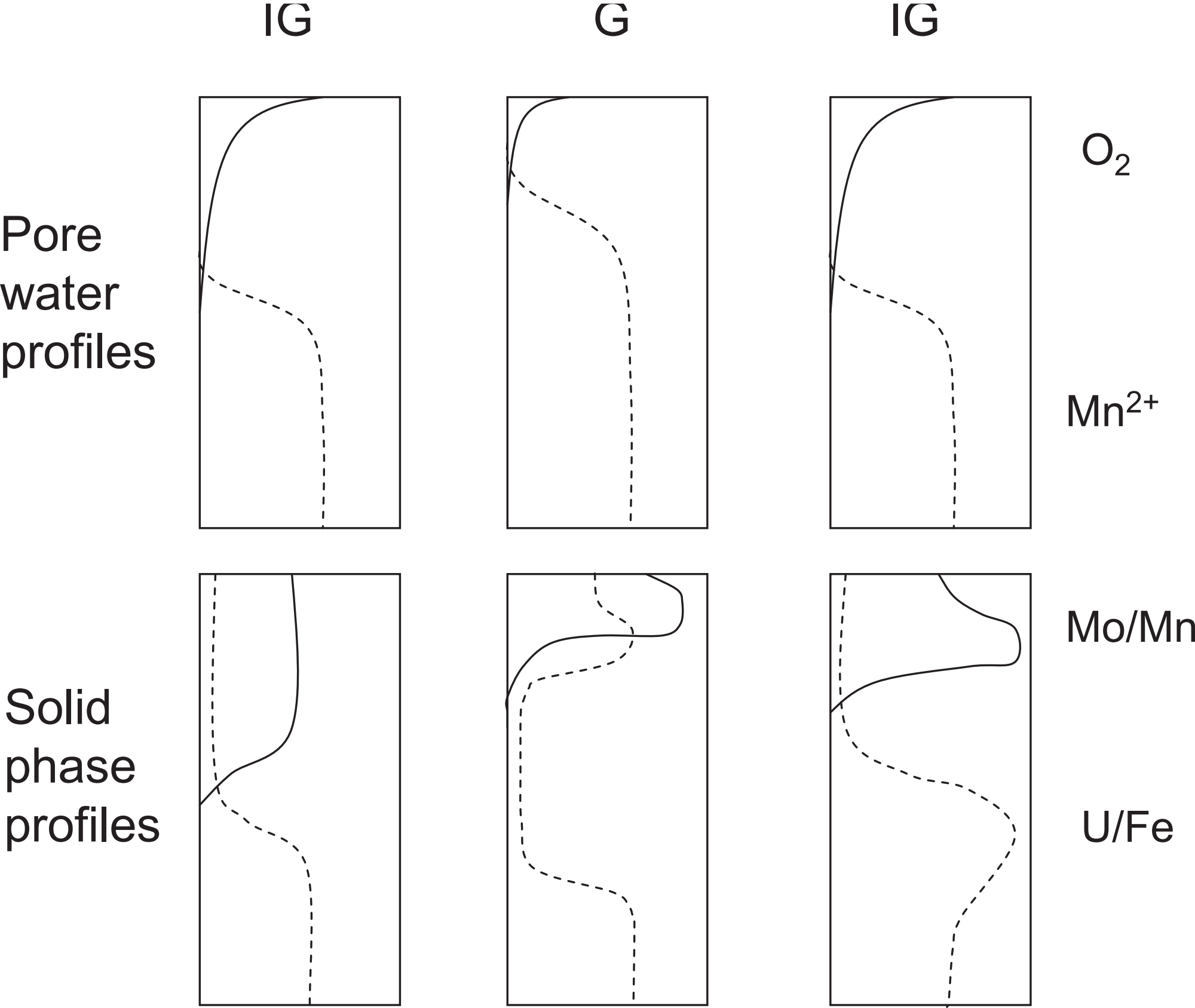
IG
G
IG
Pore water profiles
O_2
Mn^{2+}
Solid phase profiles
Mo/Mn
U/Fe

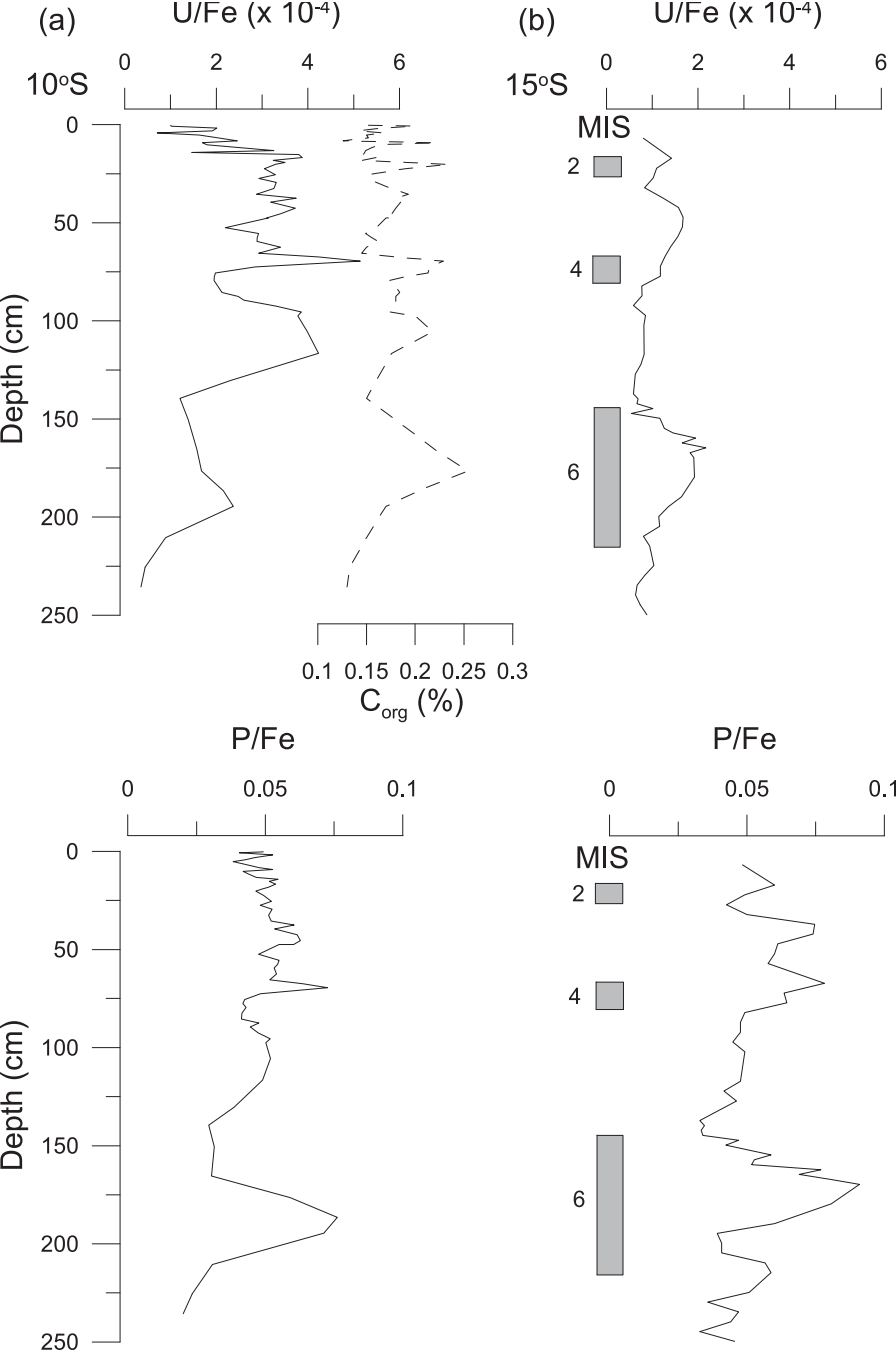
(a)
U/Fe (x 10-4)
10oS
0
2
4
6
Depth (cm)
0
50
100
150
200
250
0.1 0.15 0.2 0.25 0.3
Corg (%)
(b)
U/Fe (x 10-4)
15oS
MIS
2
4
6
P/Fe
0
0.05
0.1
MIS
2
4
6